SILVERRUSH. VIII. Spectroscopic Identifications of Early Large-scale Structures with Protoclusters over 200 Mpc at $z \sim$ 6–7: Strong Associations of Dusty Star-forming Galaxies

Yuichi Harikane[1,2,3], Masami Ouchi[1,4], Yoshiaki Ono[1], Seiji Fujimoto[1,5], Darko Donevski[6,7], Takatoshi Shibuya[8], Andreas L. Faisst[9], Tomotsugu Goto[10], Bunyo Hatsukade[11], Nobunari Kashikawa[5], Kotaro Kohno[11], Takuya Hashimoto[3,12], Ryo Higuchi[1,2], Akio K. Inoue[12], Yen-Ting Lin[13], Crystal L. Martin[14], Roderik Overzier[15,16], Ian Smail[17], Jun Toshikawa[1], Hideki Umehata[11,18], Yiping Ao[19], Scott Chapman[20], David L. Clements[21], Myungshin Im[22], Yipeng Jing[23,24], Toshihiro Kawaguchi[25], Chien-Hsiu Lee[26], Minju M. Lee[3,27], Lihwai Lin[13], Yoshiki Matsuoka[28], Murilo Marinello[15], Tohru Nagao[29], Masato Onodera[26], Sune Toft[29], and Wei-Hao Wang[13]

[1] Institute for Cosmic Ray Research, The University of Tokyo, 5-1-5 Kashiwanoha, Kashiwa, Chiba 277-8582, Japan; hari@icrr.u-tokyo.ac.jp
[2] Department of Physics, Graduate School of Science, The University of Tokyo, 7-3-1 Hongo, Bunkyo, Tokyo, 113-0033, Japan
[3] National Astronomical Observatory of Japan, 2-21-1 Osawa, Mitaka, Tokyo 181-8588, Japan
[4] Kavli Institute for the Physics and Mathematics of the Universe (WPI), University of Tokyo, Kashiwa 277-8583, Japan
[5] Department of Astronomy, Graduate School of Science, The University of Tokyo, 7-3-1 Hongo, Bunkyo, Tokyo 113-0033, Japan
[6] Aix Marseille University, CNRS, LAM, Laboratoire d'Astrophysique de Marseille, Marseille, France
[7] SISSA, via Bonomea 265, I-34136 Trieste, Italy
[8] Kitami Institute of Technology, 165 Koen-cho, Kitami, Hokkaido 090-8507, Japan
[9] Infrared Processing and Analysis Center, California Institute of Technology, MC 100-22, 770 South Wilson Ave., Pasadena, CA 91125, USA
[10] Institute of Astronomy, National Tsing Hua University, No. 101, Section 2, Kuang-Fu Road, Hsinchu, Taiwan
[11] Institute of Astronomy, Graduate School of Science, The University of Tokyo, 2-21-1 Osawa, Mitaka, Tokyo 181-0015, Japan
[12] Department of Environmental Science and Technology, Faculty of Design Technology, Osaka Sangyo University, 3-1-1, Nagaito, Daito, Osaka 574-8530, Japan
[13] Institute of Astronomy & Astrophysics, Academia Sinica, Taipei 106, Taiwan (ROC)
[14] Department of Physics, University of California, Santa Barbara, CA 93106, USA
[15] Observatorio Nacional, Rua Jose Cristino, 77. CEP 20921-400, Sao Cristovao, Rio de Janeiro-RJ, Brazil
[16] Universidade de Sao Paulo, Instituto de Astronomia, Geofísica e Ciências Atmosféricas, Departamento de Astronomia, São Paulo, SP 05508-090, Brazil
[17] Centre for Extragalactic Astronomy, Department of Physics, Durham University, South Road, Durham DH1 3LE, UK
[18] RIKEN Cluster for Pioneering Research, 2-1 Hirosawa, Wako-shi, Saitama 351-0198, Japan
[19] Purple Mountain Observatory & Key Laboratory for Radio Astronomy, Chinese Academy of Sciences, 8 Yuanhua Road, Nanjing 210034, People's Republic of China
[20] Department of Physics and Atmospheric Science, Dalhousie University, Halifax, NS B3H 3J5, Canada
[21] Astrophysics Group, Imperial College London, Blackett Laboratory, Prince Consort Road, London SW7 2AZ, UK
[22] CEOU/Astronomy Program, Dept. of Physics & Astronomy, Seoul National University, Seoul, Republic of Korea
[23] School of Physics and Astronomy, Tsung-Dao Lee Institute, Shanghai Jiao Tong University, 800 Dongchuan Road, Shanghai, 200240, People's Republic of China
[24] IFSA Collaborative Innovation Center, Shanghai Jiao Tong University, Shanghai 200240, People's Republic of China
[25] Department of Economics, Management and Information Science, Onomichi City University, Hisayamada 1600-2, Onomichi, Hiroshima 722-8506, Japan
[26] Subaru Telescope, NAOJ, 650 N Aohoku Pl, Hilo, HI 96720, USA
[27] Division of Particle and Astrophysical Science, Graduate School of Science, Nagoya University, Furo-cho, Chikusa-ku, Nagoya 464-8602, Japan
[28] Research Center for Space and Cosmic Evolution, Ehime University, Bunkyo-cho, Matsuyama, Ehime 790-8577, Japan
[29] Cosmic Dawn Center (DAWN), Niels Bohr Institute, Juliane Mariesvej 30, DK-2100 Copenhagen, Denmark

Abstract

We have obtained three-dimensional maps of the universe in $\sim 200 \times 200 \times 80$ comoving Mpc^3 (cMpc^3) volumes each at $z = 5.7$ and 6.6 based on a spectroscopic sample of 179 galaxies that achieves $\gtrsim 80\%$ completeness down to the Lyα luminosity of $\log(L_{\mathrm{Ly}\alpha}/[\mathrm{erg\ s^{-1}}]) = 43.0$, based on our Keck and Gemini observations and the literature. The maps reveal filamentary large-scale structures and two remarkable overdensities made out of at least 44 and 12 galaxies at $z = 5.692$ (z57OD) and $z = 6.585$ (z66OD), respectively, making z66OD the most distant overdensity spectroscopically confirmed to date, with >10 spectroscopically confirmed galaxies. We compare spatial distributions of submillimeter galaxies at $z \simeq 4$–6 with our $z = 5.7$ galaxies forming the large-scale structures, and detect a 99.97% signal of cross-correlation, indicative of a clear coincidence of dusty star-forming galaxy and dust-unobscured galaxy formation at this early epoch. The galaxies in z57OD and z66OD are actively forming stars with star-formation rates (SFRs) $\gtrsim 5$ times higher than the main sequence, and particularly the SFR density in z57OD is 10 times higher than the cosmic average at the redshift (a.k.a. the Madau-Lilly plot). Comparisons with numerical simulations suggest that z57OD and z66OD are protoclusters that are progenitors of the present-day clusters with halo masses of $\sim 10^{14}\ M_{\odot}$.

Key words: galaxies: evolution – galaxies: formation – galaxies: high-redshift

1. Introduction

Galaxies are not uniformly distributed in the universe. Some of them reside in groups and clusters on scales of ~ 1–3 Mpc, while others lie in long filaments of galaxies extending over 10 Mpc, called large-scale structure (e.g., Gott et al. 2005). Investigating the large-scale structure is important for understanding galaxy formation, as there is observational evidence that galaxy properties depend on their environment. Indeed, at

low redshift, galaxies in clusters are mostly passive, early-type galaxies (e.g., Dressler 1980; Goto et al. 2003), and there is a clear trend that the star-formation activity of galaxies tends to be lower in high-density environment than low-density environment (Lewis et al. 2002; Tanaka et al. 2004), known as the morphology/star formation-density relation. Because galaxies in dense environments appear to experience accelerated evolution, we need to go to higher redshifts to study the progenitors of low-redshift high-density environments.

Indeed, studies of the large-scale structure at high redshift have shown that galaxies in dense regions experience enhanced star formation (e.g., Kodama et al. 2001; Elbaz et al. 2007; Tran et al. 2010; Koyama et al. 2013), opposite to the relation at low redshift. In addition, recent cosmological simulations predict a significant increase of the contribution to the cosmic star-formation density from galaxy overdensities (Chiang et al. 2017). Thus, many galaxy overdensities have been identified and investigated at $z > 1$ to date, including protoclusters that grow to cluster-scale halos at the present day (e.g., Steidel et al. 1998, 2005; Shimasaku et al. 2003, 2004; Chiang et al. 2014, 2015; Dey et al. 2016, see Overzier 2016 for a review). At $z > 3$, as strong rest-frame optical emission lines are redshifted to mid-infrared, the Lyα emission line is used as a spectroscopic probe for galaxies. Some of the high-redshift overdense regions are identified with UV continuum and/or Lyα emission lines (e.g., Overzier et al. 2006; Utsumi et al. 2010; Toshikawa et al. 2016; Higuchi et al. 2018; Pavesi et al. 2018), and spectroscopically confirmed with Lyα (e.g., Venemans et al. 2002; Ouchi et al. 2005; Dey et al. 2016; Jiang et al. 2018), including the galaxy overdensities at $z = 6.01$ (Toshikawa et al. 2012, 2014).

Because the Lyα photons are easily absorbed by dust, it is important to investigate whether dust-obscured galaxies are also residing in high-redshift overdensities traced with the Lyα emission. In addition, dusty star-forming galaxies, such as submillimeter galaxies (SMGs), are expected to trace the most massive dark-matter halos and overdensities at $z > 2$ (e.g., Casey 2016; Béthermin et al. 2017; Miller et al. 2018). Tamura et al. (2009) report 2.2σ large-scale correlation between SMGs and Lyα emitters (LAEs) at $z = 3.1$ in the SSA22 protocluster. Umehata et al. (2014) improved the selection of SMGs using photometric redshifts, and detect stronger correlation between SMGs and LAEs in the SSA22 protocluster (see also Umehata et al. 2015, 2017, 2018). These results suggest that dust-obscured star-forming galaxies are also lying in the SSA22 protocluster traced by LAEs at $z = 3.1$. However, the association between SMGs and LAEs at higher redshift is not yet understood.

In this study, we investigate large-scale structures at $z = 5.7$ and 6.6 in the SXDS field using a large spectroscopic sample of 179 LAEs. Combined with our recent Keck/DEIMOS and Gemini/GMOS observations, we produce 3D maps of the universe traced with the LAEs in two $\sim 200 \times 200 \times 80$ cMpc^3 volumes at $z = 5.7$ and 6.6. We investigate the correlation between the LAEs and dust-obscured high-redshift SMGs, and stellar populations to probe the environmental dependence of galaxy properties. We also compare our observational results with recent numerical simulations. One of the large-scale structures investigated in this study is a protocluster at $z = 5.7$ first reported in Ouchi et al. (2005). Ouchi et al. (2005) spectroscopically confirm 15 LAEs around this protocluster. Recently, Jiang et al. (2018) studied this

protocluster with 46 spectroscopically confirmed LAEs in the SXDS field. In this study, we use 135 LAEs spectroscopically confirmed at $z = 5.7$, which allows us to obtain a more complete view of the 3D structure of this protocluster. In addition, we will investigate the correlation with high-redshift SMGs that are not investigated in these studies. This study is one in a series of papers from a program studying high-redshift galaxies, named Systematic Identification of LAEs for Visible Exploration and Reionization Research Using Subaru HSC (SILVERRUSH Ouchi et al. 2018). Early results are already reported in several papers (Harikane et al. 2018b; Higuchi et al. 2018; Inoue et al. 2018; Konno et al. 2018; Ouchi et al. 2018; Shibuya et al. 2018a, 2018b).

This paper is organized as follows. In Section 2, we present our LAE sample. We describe our spectroscopic observations in Section 3. We present our results in Section 4, and in Section 5 we summarize our findings. Throughout this paper we use the recent Planck cosmological parameter sets constrained with the temperature power spectrum, temperature-polarization cross spectrum, polarization power spectrum, low-l polarization, CMB lensing, and external data (TT, TE, EE +lowP+lensing+ext result; Planck Collaboration et al. 2016): $\Omega_m = 0.3089$, $\Omega_\Lambda = 0.6911$, $\Omega_b = 0.049$, $h = 0.6774$, and $\sigma_8 = 0.8159$. We assume a Chabrier (2003) initial mass function (IMF) with lower and upper mass cutoffs of $0.1 M_\odot$ and $100 M_\odot$, respectively. All magnitudes are in the AB system (Oke & Gunn 1983).

2. LAE Sample

We use LAE samples at $z = 5.7$ and 6.6 (Shibuya et al. 2018b) selected based on the Subaru/Hyper Suprime-Cam Subaru strategic program (HSC-SSP) survey data (Aihara et al. 2018a, 2018b), reduced with the HSC data processing pipeline (Bosch et al. 2017). The LAEs at $z = 5.7$ and 6.6 are selected with the narrowband filters $NB816$ and $NB921$, which have central wavelengths of 8170 Å and 9210 Å, and FWHMs of 131 Å and 120 Å to identify LAEs in the redshift range of $z = 5.64$–5.76 and $z = 6.50$–6.63, respectively. The HSC-SSP survey has three layers, UltraDeep (UD), Deep, and Wide, with different combinations of area and depth. In this study, we use LAE samples in the UD-SXDS field, where rich spectroscopic data are available (see Section 3). We select 224 and 58 LAEs at $z = 5.7$ and $z = 6.6$, respectively, in the UD-SXDS field with the following color criteria:

$z = 5.7$:

$$NB816 < NB816_{5\sigma} \text{ and } i - NB816 > 1.2 \text{ and}$$
$$g > g_{3\sigma} \text{ and } [(r \leqslant r_{3\sigma} \text{ and } r - i \geqslant 1.0) \text{ or } r > r_{3\sigma}], \quad (1)$$

$z = 6.6$:

$$NB921 < NB921_{5\sigma} \text{ and } z - NB921 > 1.0 \text{ and}$$
$$g > g_{3\sigma} \text{ and } r > r_{3\sigma} \text{ and}$$
$$[(z \leqslant z_{3\sigma} \text{ and } i - z \geqslant 1.3) \text{ or } z > z_{3\sigma}]. \quad (2)$$

The subscripts "5σ" and "3σ" indicate the 5σ and 3σ magnitude limits for a given filter, respectively. Based on spectroscopic observations in Shibuya et al. (2018a), the contamination rate is 0%–30%. In addition, we use fainter LAE samples at $z = 5.7$ and 6.6 selected with Subaru/Suprime-Cam
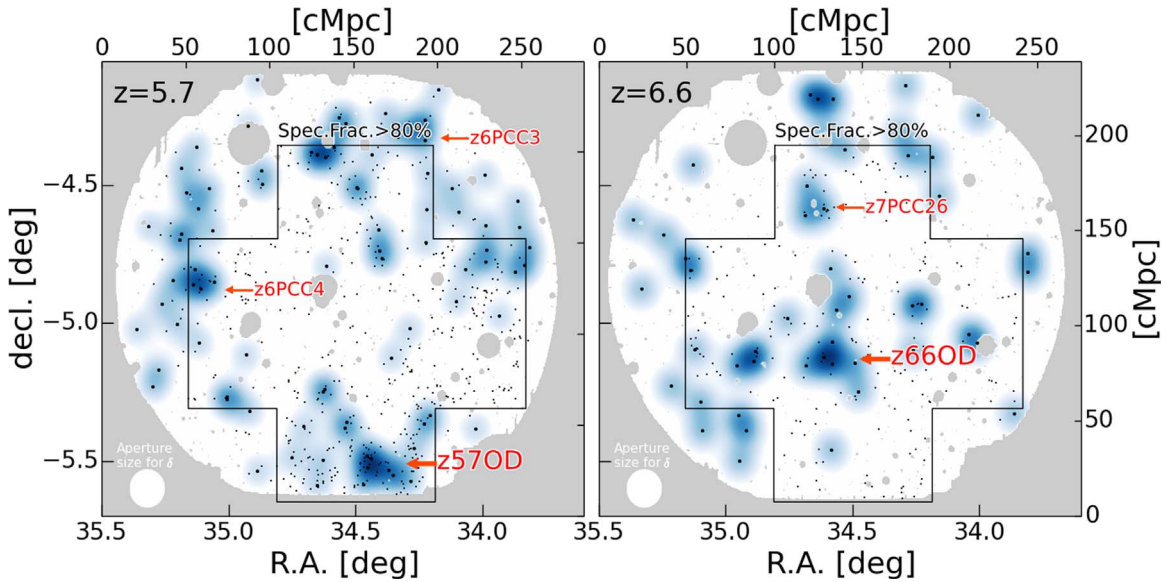
Figure 1. Overdensity maps of LAEs at $z = 5.7$ (left) and $z = 6.6$ (right). The black dots show the positions of the LAEs. The large dots are LAEs whose *NB* magnitudes are brighter than 24.5 and 25.0 at $z = 5.7$ and 6.6, respectively. The blue contours show number densities of LAEs brighter than 24.5 and 25.0 at $z = 5.7$ and 6.6, respectively. Higher-density regions are indicated by the darker colors. The gray regions are masked due to the survey edges and bright stars. The region indicated by the black polygon is the region where the fraction of spectroscopically confirmed LAEs brighter than $L_{Ly\alpha} > 10^{43}$ erg s^{-1} is $\gtrsim 80\%$.

images in Ouchi et al. (2008, 2010). The total numbers of LAEs are 563 and 247 at $z = 5.7$ and 6.6, respectively.

To identify LAE overdensities, we calculate the galaxy overdensity, δ, that is defined as follows:

$$\delta = \frac{n - \bar{n}}{\bar{n}}, \quad (3)$$

where n is the number of LAEs in a cylinder and $\bar{n}$ is its average. To draw two-dimensional (2D) projected overdensity contours, we choose a cylinder whose height is ~ 40 cMpc corresponding to the redshift range of the narrowband-selected LAEs at each redshift. The radius of the cylinder is 0.07 deg, which corresponds to ~ 10 cMpc at $z \sim 6$, which is a typical size of the protoclusters growing to $\sim 10^{15}\ M_\odot$ halo at $z = 0$ in simulations in Chiang et al. (2013). We use LAEs brighter than $NB816 < 24.5$ and $NB921 < 25.0$ at $z = 5.7$ and 6.6, respectively, to keep high detection completeness. The average numbers of LAEs in a cylinder are $\bar{n} = 0.48$ and 0.26 at $z = 5.7$ and 6.6, respectively. The masked regions are excluded in the calculations. In Figure 1, we plot the calculated overdensities smoothed with a Gaussian kernel of $\sigma = 0.07$ deg. Here, we define overdensities as regions whose overdensity significances are higher than 4σ levels. We identify overdensities previously reported in Higuchi et al. (2018); z6PCC1, z6PCC3, and z6PCC4 at $z = 5.7$, and z7PCC24 and z7PCC26 (see also Chanchaiworawit et al. 2017, 2019) at $z = 6.6$.[30] z6PCC1 is the same structure reported in Ouchi et al. (2005) and Jiang et al. (2018, see Section 4.1). Hereafter, we refer to z6PCC1 ($n = 6$, $\delta = 11.5$, 7.2σ) and z7PCC24 ($n = 4$, $\delta = 14.3$, 6.8σ), the most overdense regions at $z = 5.7$ and 6.6 in the UD-SXDS field, as z57OD and z66OD, respectively.

3. Spectroscopic Data

Out of 563 and 247 LAEs at $z = 5.7$ and 6.6, 135 and 36 LAEs are spectroscopically confirmed, respectively, in previous studies (Ouchi et al. 2005, 2008, 2010; Harikane et al. 2018b; Higuchi et al. 2018; Jiang et al. 2018; Shibuya et al. 2018a). Four LAEs around z66OD, z66LAE-1, -2, -3, and -4 are already spectroscopically confirmed. In addition, we conducted Gemini and Keck spectroscopy targeting LAEs of z66OD.

We used Gemini Multi-Object Spectrographs (GMOS) on the 8 m Gemini North telescope in 2017 and 2018. We used a total of two GMOS masks with the OG515 filter and R831 grating, and the total exposure times were 5400 and 10,220 s. Our exposures were conducted with spectral dithering of 50 Å to fill CCD gaps. The spectroscopic coverage was between 7900 and 10000 Å. The spatial pixel scale was 0″0727 pixel^{-1}. The slit width was 0″75 and the spectral resolution was $R \sim 3000$. The seeing was around 0″9. The reduction was performed using the Gemini IRAF packages.[31] Wavelength calibration was achieved by fitting to the OH emission lines.

We also used DEep Imaging Multi-Object Spectrograph (DEIMOS) on the 10 m Keck II telescope in 2018. We used one DEIMOS mask with the OG550 filter and 830G grating, and the total exposure time was 4900 s. The spectroscopic coverage was between 6000 and 10000 Å. The spatial pixel scale was 0″1185 pixel^{-1}. The slit width was 0″8 and the spectral resolution was $R \sim 3000$. The seeing was around 0″8. The reduction was performed using the spec2d IDL pipeline developed by the DEEP2 Redshift Survey Team (Davis et al. 2003). Wavelength calibration was achieved by fitting to the arc lamp emission lines.

In these observations, we identified emission lines in eight LAEs, z66LAE-5, -6, -7, -8, -9, -10, -11, and -12. We evaluate asymmetric profiles of these emission lines by calculating the weighted skewness, S_w (Kashikawa et al. 2006).

---

[30] We regard z7PCC26 as an overdensity following Higuchi et al. (2018).

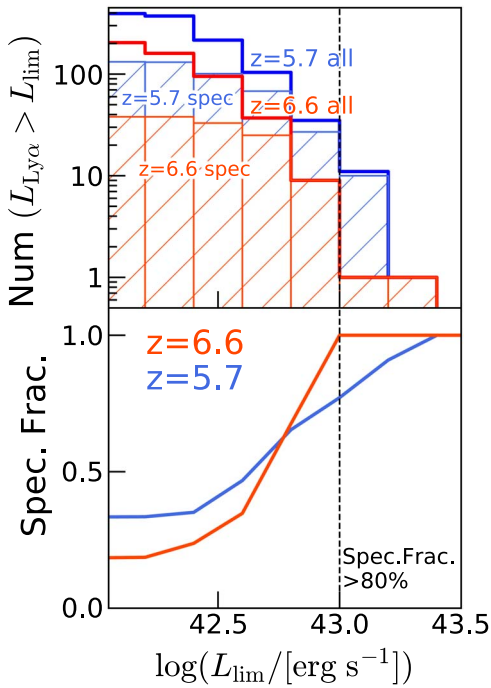[31] https://www.gemini.edu/sciops/data-and-results/processing-software

Figure 2. Upper panel: number of LAEs with spectroscopic confirmations. The blue and red histograms show cumulative numbers of all LAEs (open histogram) and spectroscopically confirmed LAEs (hatched histogram) in the black pentagon in Figure 1 at $z = 5.7$ and 6.6, respectively. Lower panels: fraction of spectroscopically confirmed LAEs at $z = 5.7$ and 6.6. The blue and red solid curves show cumulative fractions of spectroscopically confirmed LAEs in the black pentagon in Figure 1 at $z = 5.7$ and 6.6, respectively.

We find that the weighted skewness values of the lines in six LAEs, z66LAE-5, -6, -7, -8, -10, and -11 are larger than 3, indicating that these asymmetric lines are Lyα. The weighted skewness values of the lines in z66LAE-9 and z66LAE-12 are less than 3. The narrow emission lines (FWHM $\simeq 200$ km s^{-1} after a correction for the instrumental broadening) and medium spectral resolution ($R \sim 3000$) do not suggest that these emission lines are [O II]$\lambda\lambda$3726, 3729. We do not find significant emission lines except for these lines at $\sim$9190 and $\sim$9250 Å, rejecting the possibility of [O III]λ5007 emitters with detectable [O III]λ4959 or Hβ lines, or Hα emitters with a detectable [O III]λ5007 line. Since most unresolved single line emitters have been found to be LAEs with a moderate velocity dispersion (Hu et al. 2004), we regard these lines as Lyα. Note that removing z66LAE-9 and z66LAE-12 from our analysis does not change our conclusions.

Thus, a total of 135 and 44 spectroscopically confirmed LAEs at $z = 5.7$ and 6.6 are used in this study. Figure 2 shows the numbers of LAEs spectroscopically confirmed and their fractions. Thanks to the large spectroscopic sample, the fraction of the spectroscopically confirmed LAEs is $\gtrsim$80% down to the Lyα luminosity of $L_{\text{Ly}\alpha} = 10^{43}$ erg s^{-1} at $z = 5.7$ and 6.6 in the regions indicated with the black polygon in Figure 1, corresponding to the SXDS fields in Ouchi et al. (2008, 2010). Although the spectroscopic fraction of z57OD (88% for $L_{\text{Ly}\alpha} > 10^{43}$ erg s^{-1}) is higher than that of all $z = 5.7$ LAEs (77% for $L_{\text{Ly}\alpha} > 10^{43}$ erg s^{-1}), the difference ($\sim$10%) is not significant for our identifications of the overdensities in Section 4.1. We do not find strong AGN signatures, such as broad Lyα emission lines or N V 1240 lines, in the spectra of our LAEs.

4. Results and Discussions

4.1. Large-scale Structure at z = 5.7 and z = 6.6 and Spectroscopic Confirmation of z66OD at z = 6.585

We obtain the three-dimensional (3D) map using the 179 spectroscopic confirmed LAEs. We calculate the 3D over-density using the LAE sample with a sphere whose radius is 10 cMpc (15 cMpc) at $z = 5.7$ ($z = 6.6$). Note that velocity offsets of the Lyα emission lines to the systemic redshifts are typically $\sim$300 km s^{-1} or $\sim$2.5 cMpc (e.g., Erb et al. 2014; Faisst et al. 2016; Hashimoto et al. 2018), smaller than the radius of the sphere. In Figure 3, we plot the locations of the LAEs and the 3D overdensity smoothed with a Gaussian kernel of $\sigma = 10$ cMpc (15 cMpc) at $z = 5.7$ ($z = 6.6$). Figure 4 shows the 2D maps with the redshift slices of $\Delta z \sim 0.02$. These maps reveal the filamentary 3D large-scale structures made by the LAEs at $z = 5.7$ and 6.6.

In the 3D maps, we identify z57OD ($z = 5.692$) and z66OD ($z = 6.585$) with 44 and 12 LAEs spectroscopically confirmed, respectively, which are located within $\sim$1σ contours in Figures 5 and 6. The 1σ contours are roughly corresponding to the 20 cMpc-radius aperture. According to theoretical studies in Chiang et al. (2017), the 20 cMpc-radius aperture at $z \sim 6$ includes >90% members of clusters at $z = 0$. We include z66LAE-8 located just outside the 1σ contour, because it is within 20 cMpc from the center of z66OD. Figures 5 and 6 show the locations of LAEs, 2D projected contours, and spectra of the LAEs of z57OD and z66OD, respectively. Tables 1 and 2 summarize properties of LAEs of z57OD and z66OD, respectively. The average redshift of the LAEs of z66OD ($z = 6.585$) suggests that z66OD is the most distant overdensity with >10 galaxies spectroscopically confirmed to date (see, 3 galaxies at $z = 7.1$ in Castellano et al. 2018). Properties of overdensities in this work and in the literature are summarized in Table 3, which is based on objects listed in Table 5 in Chiang et al. (2013) and new objects discovered since.

Both z57OD and z66OD are located in the filamentary structures made by LAEs around these overdensities, extending over 40 cMpc. We evaluate the extension of these overdensities in the redshift direction by calculating velocity dispersions of LAEs. We select LAEs within 0.07 deg from the centers (defined as the highest density peaks) of z57OD and z66OD, and calculate the rms of their velocities as velocity dispersions. The calculated velocity dispersions are 1280 ± 220 km s^{-1} and 670 ± 200 km s^{-1}, respectively, similar to the value of galaxies in overdensities found in Lemaux et al. (2018, 1038 ± 178 km s^{-1}) and Toshikawa et al. (2012, 647 ± 124 km s^{-1}), respectively. These velocity dispersions are compared with simulations in Section 4.2.

Jiang et al. (2018) identify SXDS_gPC in their spectroscopic survey. Since the coordinate and redshift of SXDS_gPC are the same as those of z57OD, we conclude that SXDS_gPC is the same structure as z57OD. Jiang et al. (2018) spectroscopically confirm 46 LAEs at $z = 5.7$ in the UD-SXDS field. 34 LAEs among the 46 LAEs overlap with our LAE catalog, and traces similar large-scale structures to the ones we identify. However, the overdensity value and its significance ($\delta = 5.6$, $\sim$5σ) are different from our measurements ($\delta = 15.0$, 8.4σ). This is because the aperture size and magnitude limit of LAEs for the δ calculation are different between our measurements (10 cMpc-radius circular aperture and 24.5 mag) and Jiang et al. (35^2 cMpc^2 aperture and 25.5 mag). If we calculate by adopting
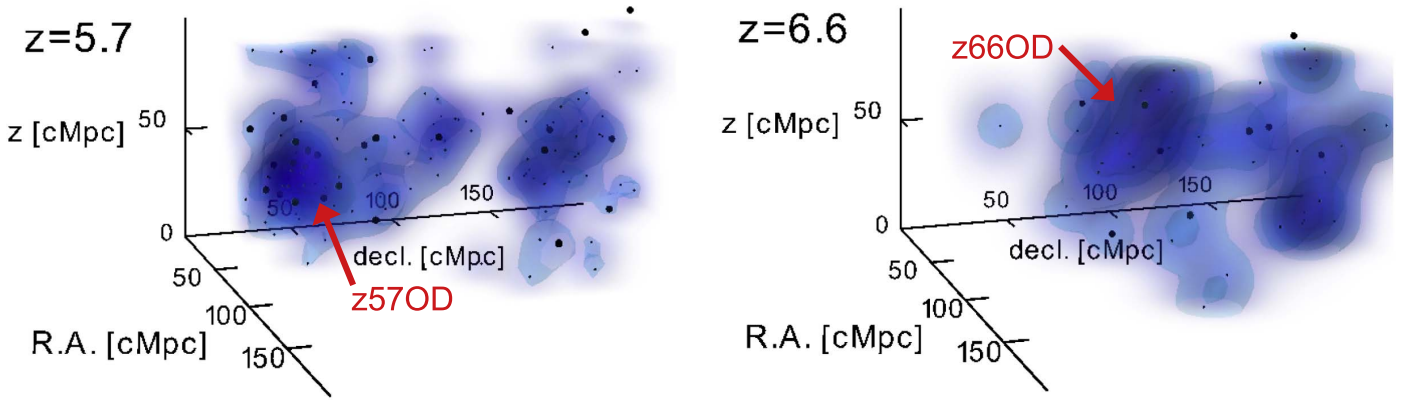
Figure 3. 3D overdensity maps of LAEs at $z = 5.7$ (left) and $z = 6.6$ (right). The black dots show the positions of the LAEs. The large dots are LAEs brighter than $L_{Ly\alpha} > 10^{43}$ erg s^{-1}. Higher-density regions are indicated by the bluer colors, smoothed with a Gaussian kernel of $\sigma = 10$ cMpc (15 cMpc) at $z = 5.7$ ($z = 6.6$).
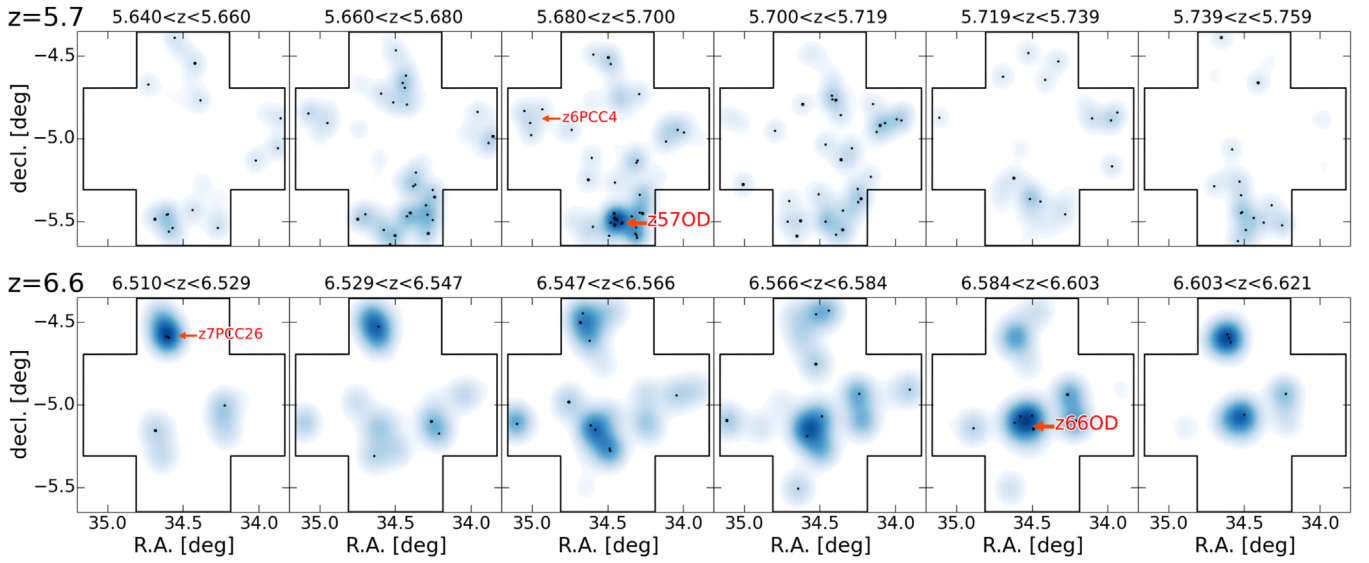

Figure 4. Two-dimensional map of LAEs at $z = 5.7$ (upper) and $z = 6.6$ (lower) with the redshift slices. The black dots show the positions of the LAEs in the $\Delta z \sim 0.02$ redshift depth. The large dots are LAEs brighter than $L_{Ly\alpha} > 10^{43}$ erg s^{-1}. Higher-density regions are indicated by the darker colors, smoothed with a Gaussian kernel of $\sigma = 10$ cMpc (15 cMpc) at $z = 5.7$ ($z = 6.6$).

the same aperture size and magnitude limit as Jiang et al. (2018) for spectroscopically confirmed LAEs, we obtain $\delta = 4.8$ (4.1σ), comparable to the measurements of Jiang et al. (2018).

4.2. Comparison with Simulations

We compare our results with numerical simulations of Inoue et al. (2018) to estimate halo masses of z57OD and z66OD. Inoue et al. (2018) use N-body simulations with 4096^3 dark-matter particles in a comoving box of 162 Mpc. The particle mass is 2.46×10^6 $M_\odot$ and the minimum halo mass is 9.80×10^7 $M_\odot$. Halos' ionizing emissivity and IGM H I clumpiness are produced by an RHD simulation with a 20 comoving Mpc^3 box (K. Hasegawa et al. 2019, in preparation). LAEs have been modeled with physically motivated analytic recipes as a function of halo mass. LAEs are modeled based on the radiative transfer calculations by a radiative hydrodynamic simulation (K. Hasegawa et al. 2019, in preparation). In this work, we use the LAE model G with the late reionization history, which reproduces all observational results, namely the neutral hydrogen fraction measurements, Lyα luminosity

functions, LAE angular correlation functions, and Lyα fractions in LBGs at $z \gtrsim 6$. Thus, we expect that similar systems to z57OD and z66OD are found in the simulations. We slice the $162 \times 162 \times 162$ cMpc^3 box into four slices of $162 \times 162 \times 40.5$ cMpc^3 whose depth ($\sim$40 cMpc) is comparable to the redshift range of the narrowband-selected LAEs at $z = 5.7$ and 6.6. Magnitudes of the LAEs are calculated based on the transmission curves of the HSC filters.

We select $z = 5.7$ and 6.6 mock LAEs with $i - NB816 > 1.2$ and $z - NB921 > 1.0$, which are the same as our color criteria of Equations (1) and (2), respectively. Then we use mock LAEs brighter than $NB816 < 24.5$ mag and $NB921 < 25.0$ mag at $z = 5.7$ and 6.6, respectively, and calculate the galaxy overdensity in each slice with a cylinder whose depth and radius are 40 cMpc and 10 cMpc, respectively. The average number densities of LAEs in the cylinder are $\bar{n} = 0.39$ and 0.32 at $z = 5.7$ and 6.6, respectively, which agree with observations within 1σ fluctuations. We show the calculated overdensity in each slice in Figure 7. We define overdensities as regions whose overdensity significances are higher than 4σ. We calculate velocity dispersions of LAEs in
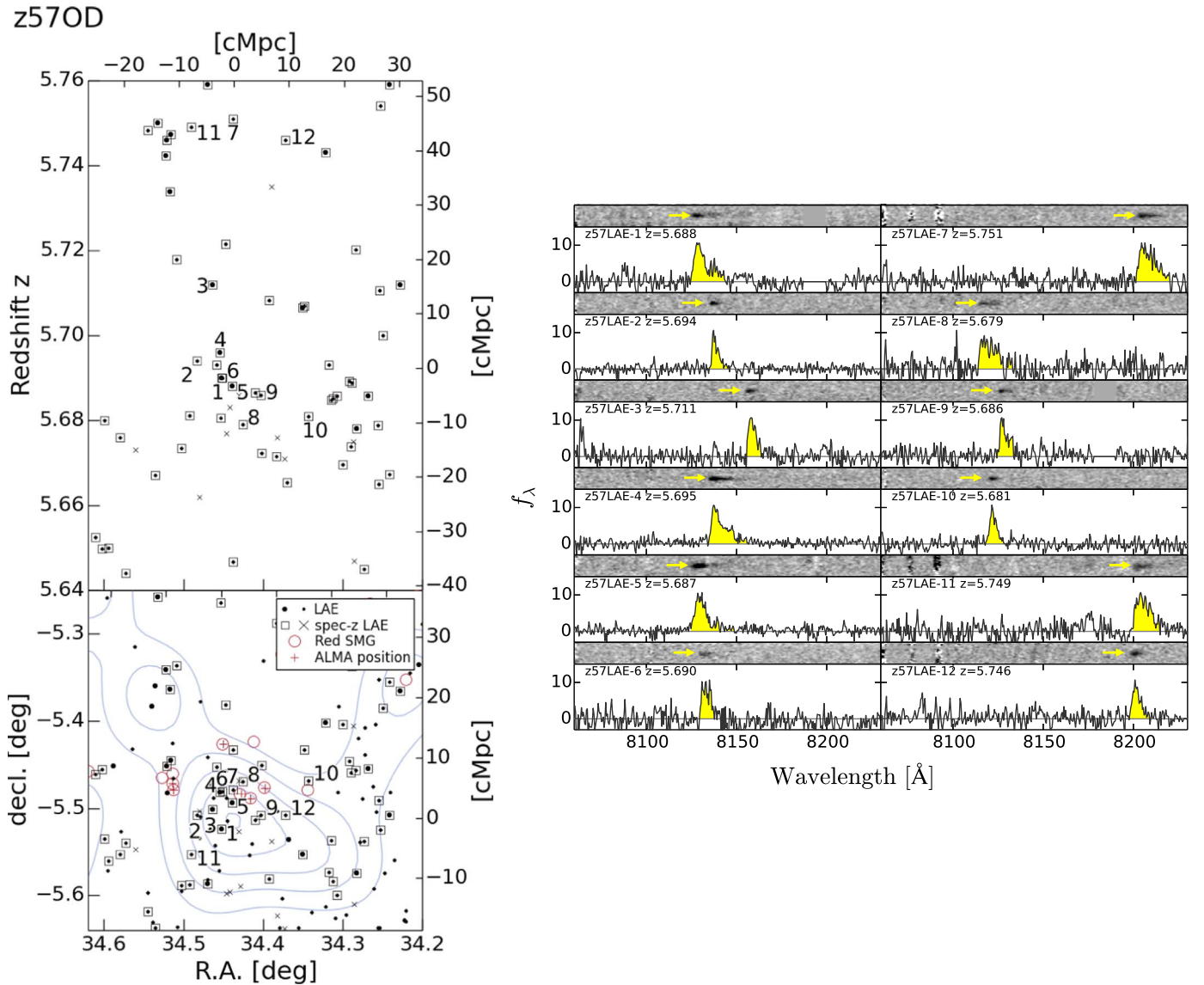
Figure 5. Left panel: 3D distribution of LAEs of z57OD. The large dots are LAEs whose *NB* magnitudes are brighter than 24.5. The LAEs indicated with the black squares are spectroscopically confirmed. The crosses are spectroscopically confirmed LAEs in Jiang et al. (2018) that are not identified in our photometric catalog. The numbers denote IDs of the LAEs. The cyan contour shows the significance levels of the overdensity from 1σ to 5σ. The red circles are the red SMGs (see Section 4.3), and the red crosses show the positions of the ALMA counterparts of the SMGs. Right panel: examples of spectra of LAEs of z57OD. The y-axis ranges of the 2D spectra are $\pm 5''$. The y-axes in the 1D spectra are arbitrary.

the overdensities, using LAEs within 10 cMpc from the centers of the overdensities, a similar aperture size to the one used in the velocity dispersion calculations for z57OD and z66OD.

We compare the significances and velocity dispersions of the overdensities in the simulations with z57OD and z66OD in Figure 8. At $z = 5.7$, we find three overdensities, simOD1 ($\delta = 19.5$, 10.8σ, $\sigma_V = 1100$ km s^{-1}), simOD2 ($\delta = 11.8$, 6.6σ, $\sigma_V = 750$ km s^{-1}), and simOD3 ($\delta = 9.3$, 5.1σ, $\sigma_V = 1500$ km s^{-1}), whose significance and velocity dispersion are comparable with z57OD with $\lesssim 2\sigma$ uncertainties. The masses of the most massive halos in these three overdensities are 1.0×10^{12} $M_\odot$, 4.7×10^{11} $M_\odot$, and 7.7×10^{11} $M_\odot$, respectively, at $z = 5.7$. At $z = 6.6$, we identify one overdensity, simOD4 ($\delta = 13.7$, 7.3σ, $\sigma_V = 610$ km s^{-1}), whose significance and velocity dispersion are comparable with z66OD with $\lesssim 1\sigma$ uncertainties. The mass of the most massive halo in simOD4 is 3.9×10^{11} $M_\odot$ at $z = 6.6$. Because the simulations do not go to $z \sim 0$, we use the extended Press–Schechter model of

Hamana et al. (2006) to estimate the present-day halo masses of the $z = 5.7$ and 6.6 halos. We find that these four overdensities in the simulations will grow to the cluster-scale halo ($M_h \sim 10^{14}$ $M_\odot$) at $z \sim 0$ with scatters of ~ 1 dex in M_h, indicating that z57OD and z66OD are protoclusters. Note that Overzier et al. (2009) reached the same conclusion on the progenitor of z57OD.

We also estimate present-day halo masses of z57OD and z66OD using another method following previous studies (Steidel et al. 1998; Venemans et al. 2005; Toshikawa et al. 2012). The halo mass at $z = 0$ of a protocluster M_h is given by

$$M = \bar{\rho} V (1 + \delta_m), \qquad (4)$$

where $\bar{\rho} = 4.1 \times 10^{10}$ $M_\odot$ Mpc^{-3} is the mean matter density of the universe, V is the comoving volume of the protocluster that collapses into the cluster at $z = 0$, and δ_m is the mass overdensity. The mass overdensity δ_m is related to the galaxy
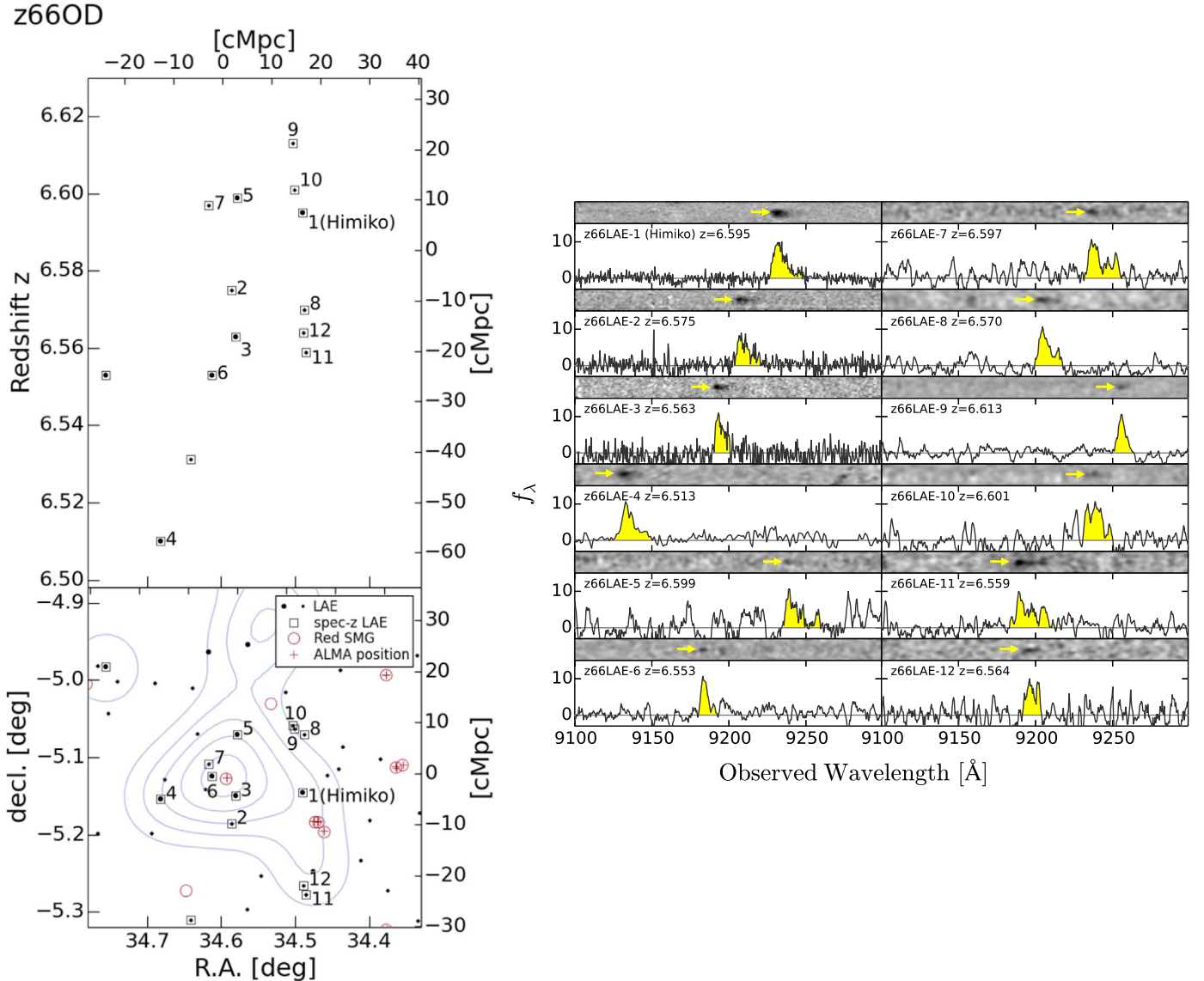
Figure 6. Same as Figure 5 but for z66OD. The large dots are LAEs whose *NB* magnitudes are brighter than 25.0. The signals in the 2D spectra of z66LAE-4 (∼9270 Å) and z66LAE-8 (∼9160 Å) are residuals of the sky subtractions.

overdensity δ with

$$1 + b\delta_{\rm m} = C(1 + \delta), \qquad (5)$$

where b is the bias factor of galaxies and C is the correction factor for the redshift space distortion. We assume $C = 1$ because this value is close to 1 at high redshift (Lahav et al. 1991). The biases of LAEs at $z = 5.7$ and 6.6 are estimated to be $b = 4.1$ and $b = 4.5$ in Ouchi et al. (2018). Assuming $V = (4/3)\pi \times 10^3$ Mpc^3 (typical size of a protocluster in Chiang et al. 2013), we estimate the present-day halo masses of z57OD and z66OD to be $4.8 \times 10^{14} M_\odot$ and $5.4 \times 10^{14} M_\odot$, which agree with those estimated with the simulations. These estimated present-day halo masses support that z57OD and z66OD are protoclusters.

As discussed in the previous paragraph, we identify similar overdensities to z57OD in the simulation. However, Jiang et al. (2018) report that they do not find overdensities similar to z57OD in their cosmological simulation that is an update of a previous work (Chiang et al. 2013). This difference may be due

to the different sizes of apertures used to search overdensities. We use a 10 cMpc-radius circular aperture, while Jiang et al. (2018) use a larger, 35^2 cMpc^2 aperture. Thus, the simulations could reproduce overdensities on a small scale, but not on a large scale.

4.3. Correlation with Red SMGs

In Section 4.1, we identify the large-scale structures made by LAEs, typically dust-poor star-forming galaxies. It is important to investigate whether dust-obscured star formation also traces the large-scale structures. We select high-redshift SMGs at $z \simeq 4$–6 (hereafter red SMGs) from the JCMT/SCUBA-2 Cosmology Legacy Survey 850 μm source catalog (Geach et al. 2017) using *Herschel*/SPIRE fluxes. It should be noted that ∼850 μm offers the negative K-correction to study SMGs with the same sensitivity at $z \sim 6$ as at the $z = 2$–3.

To estimate *Herschel*/SPIRE fluxes and partially overcome a confusion problem due to the large beam size, we apply a deblending approach using higher-resolution positional priors.

Table 1
Spectroscopically Confirmed LAEs of z57OD

ID (1)	R.A. (J2000) (2)	Decl. (J2000) (3)	$z_{\rm spec}$ (4)	$\log L_{\rm Ly\alpha}$ (5)	$M_{\rm UV}$ (6)	$EW^0_{\rm Ly\alpha}$ (7)	Reference (8)
z57LAE-1	02:17:48.46	−05:31:27.02	5.688	$43.06^{+0.04}_{-0.05}$	$-20.9^{+0.3}_{-0.2}$	54^{+22}_{-13}	O08
z57LAE-2	02:17:55.83	−05:30:26.94	5.694	$42.57^{+0.10}_{-0.13}$	$-18.9^{+1.1}_{-1.1}$	86^{+162}_{-38}	Hi18
z57LAE-3	02:17:51.14	−05:30:03.64	5.711	$42.74^{+0.08}_{-0.10}$	$-19.6^{+0.8}_{-0.7}$	86^{+103}_{-43}	O08
z57LAE-4	02:17:49.11	−05:28:54.17	5.695	$43.17^{+0.03}_{-0.04}$	$-19.8^{+0.8}_{-0.6}$	193^{+206}_{-83}	O08
z57LAE-5	02:17:45.24	−05:29:36.01	5.687	$43.09^{+0.04}_{-0.04}$	>-19.4	>216	O08
z57LAE-6	02:17:48.19	−05:28:51.92	5.690	$42.59^{+0.09}_{-0.12}$	$-18.9^{+1.1}_{-1.1}$	99^{+200}_{-49}	Hi18
z57LAE-7	02:17:45.01	−05:28:42.37	5.751	$42.71^{+0.09}_{-0.11}$	$-20.7^{+0.2}_{-0.2}$	30^{+12}_{-8}	O08
z57LAE-8	02:17:42.17	−05:28:10.55	5.679	$42.91^{+0.06}_{-0.07}$	$-20.8^{+0.2}_{-0.2}$	46^{+16}_{-11}	Hi18
z57LAE-9	02:17:36.68	−05:30:27.57	5.686	$42.53^{+0.11}_{-0.14}$	$-18.9^{+1.1}_{-1.1}$	88^{+156}_{-46}	Hi18
z57LAE-10	02:17:22.28	−05:28:05.30	5.681	$42.76^{+0.06}_{-0.08}$	$-18.9^{+1.1}_{-1.1}$	151^{+228}_{-69}	Hi18
z57LAE-11	02:17:57.66	−05:33:09.16	5.749	$42.75^{+0.10}_{-0.12}$	$-20.0^{+0.6}_{-0.6}$	66^{+89}_{-29}	Hi18
z57LAE-12	02:17:29.18	−05:30:28.50	5.746	$42.48^{+0.13}_{-0.19}$	$-19.1^{+1.0}_{-1.0}$	66^{+124}_{-36}	Hi18
z57LAE-13	02:16:54.60	−05:21:55.53	5.712	$43.10^{+0.04}_{-0.04}$	$-20.1^{+0.7}_{-0.5}$	127^{+129}_{-48}	Hi18
z57LAE-14	02:17:04.30	−05:27:14.30	5.686	$43.15^{+0.04}_{-0.04}$	$-20.3^{+0.6}_{-0.4}$	119^{+102}_{-40}	Hi18
z57LAE-15	02:17:07.85	−05:34:26.51	5.678	$43.24^{+0.03}_{-0.03}$	$-20.6^{+0.4}_{-0.3}$	113^{+64}_{-31}	Hi18
z57LAE-16	02:17:24.02	−05:33:09.62	5.707	$43.32^{+0.02}_{-0.02}$	$-21.3^{+0.2}_{-0.2}$	75^{+20}_{-14}	Hi18
z57LAE-17	02:18:03.87	−05:26:43.45	5.747	$42.90^{+0.06}_{-0.07}$	>-19.4	>136	Hi18
z57LAE-18	02:18:04.17	−05:21:47.25	5.734	$42.87^{+0.06}_{-0.08}$	$-21.4^{+0.2}_{-0.2}$	23^{+7}_{-5}	Hi18
z57LAE-19	02:18:05.17	−05:27:04.06	5.746	$42.89^{+0.06}_{-0.07}$	>-19.4	>133	Hi18
z57LAE-20	02:18:05.28	−05:20:26.89	5.742	$42.80^{+0.08}_{-0.09}$	$-20.5^{+0.5}_{-0.3}$	44^{+33}_{-16}	Hi18
z57LAE-21	02:18:28.87	−05:14:23.01	5.737	$43.38^{+0.02}_{-0.02}$	$-20.4^{+0.6}_{-0.4}$	198^{+161}_{-64}	Hi18
z57LAE-22	02:18:30.53	−05:14:57.80	5.688	$43.27^{+0.03}_{-0.03}$	$-20.4^{+0.6}_{-0.4}$	154^{+124}_{-50}	Hi18
z57LAE-23	02:17:13.81	−05:35:58.23	5.686	$42.86^{+0.09}_{-0.11}$	$-21.0^{+0.3}_{-0.3}$	33^{+15}_{-10}	Hi18
z57LAE-24	02:18:00.70	−05:35:18.92	5.673	$43.04^{+0.05}_{-0.06}$	$-21.6^{+0.1}_{-0.1}$	28^{+6}_{-5}	Hi18
z57LAE-25	02:17:58.09	−05:35:15.35	5.681	$42.55^{+0.11}_{-0.14}$	$-19.0^{+1.0}_{-1.0}$	82^{+134}_{-41}	Hi18
z57LAE-26	02:17:14.93	−05:35:02.77	5.685	$42.50^{+0.12}_{-0.17}$	$-20.6^{+0.2}_{-0.2}$	20^{+10}_{-7}	Hi18
z57LAE-27	02:17:34.16	−05:34:52.56	5.708	$42.63^{+0.09}_{-0.11}$	$-18.9^{+1.1}_{-1.1}$	105^{+221}_{-48}	Hi18
z57LAE-28	02:17:16.10	−05:34:24.23	5.693	$42.73^{+0.08}_{-0.10}$	$-19.1^{+1.1}_{-1.1}$	118^{+239}_{-59}	Hi18
z57LAE-29	02:17:05.63	−05:32:17.66	5.645	$42.89^{+0.08}_{-0.09}$	$-20.7^{+0.3}_{-0.3}$	48^{+27}_{-14}	Hi18
z57LAE-30	02:17:15.53	−05:32:14.04	5.685	$42.51^{+0.11}_{-0.15}$	$-19.9^{+0.4}_{-0.4}$	38^{+31}_{-15}	Hi18
z57LAE-31	02:17:38.28	−05:30:48.70	5.687	$42.86^{+0.07}_{-0.09}$	$-19.9^{+0.6}_{-0.6}$	85^{+90}_{-33}	Hi18
z57LAE-32	02:17:01.13	−05:29:28.40	5.665	$42.53^{+0.12}_{-0.17}$	$-19.1^{+1.1}_{-1.1}$	72^{+141}_{-39}	Hi18
z57LAE-33	02:17:09.50	−05:27:31.49	5.674	$42.71^{+0.08}_{-0.10}$	$-19.1^{+1.1}_{-1.1}$	125^{+235}_{-66}	Hi18
z57LAE-34	02:17:07.96	−05:27:23.16	5.720	$42.52^{+0.12}_{-0.17}$	$-19.1^{+1.1}_{-1.1}$	68^{+136}_{-36}	Hi18
z57LAE-35	02:17:49.99	−05:27:08.07	5.693	$43.08^{+0.06}_{-0.07}$	$-20.3^{+0.6}_{-0.6}$	104^{+116}_{-40}	O08
z57LAE-36	02:17:36.38	−05:27:01.62	5.672	$43.16^{+0.04}_{-0.05}$	$-20.2^{+0.5}_{-0.5}$	136^{+105}_{-47}	Hi18
z57LAE-37	02:17:09.95	−05:26:46.53	5.689	$42.91^{+0.07}_{-0.09}$	$-19.4^{+1.1}_{-1.1}$	126^{+230}_{-58}	Hi18
z57LAE-38	02:17:45.19	−05:25:57.75	5.647	$42.59^{+0.11}_{-0.15}$	$-19.7^{+0.6}_{-0.6}$	56^{+68}_{-26}	Hi18
z57LAE-39	02:16:59.94	−05:23:05.33	5.700	$42.49^{+0.12}_{-0.16}$	$-19.8^{+0.5}_{-0.5}$	40^{+40}_{-17}	Hi18
z57LAE-40	02:16:57.88	−05:21:16.99	5.667	$43.16^{+0.04}_{-0.04}$	$-19.7^{+0.8}_{-0.8}$	210^{+311}_{-89}	Hi18
z57LAE-41	02:18:02.18	−05:20:11.48	5.718	$42.59^{+0.09}_{-0.12}$	$-18.9^{+1.1}_{-1.1}$	99^{+167}_{-49}	Hi18
z57LAE-42	02:17:01.43	−05:18:41.68	5.679	$42.71^{+0.08}_{-0.09}$	$-19.0^{+1.1}_{-1.1}$	118^{+202}_{-55}	Hi18
z57LAE-43	02:17:00.61	−05:31:30.27	5.754	$42.56^{+0.11}_{-0.14}$	$-20.0^{+0.5}_{-0.5}$	44^{+39}_{-18}	J18
z57LAE-44	02:17:52.63	−05:35:11.79	5.759	$43.49^{+0.02}_{-0.02}$	$-22.1^{+0.1}_{-0.1}$	50^{+6}_{-5}	J18

Note. (1) Object ID. (2) Right ascension. (3) Declination. (4) Spectroscopic redshift of the Lyα emission line. (5) Lyα luminosity in units of erg s^{-1}. (6) Absolute UV magnitude or its 2σ lower limit in units of ABmag. (7) Rest-frame Lyα EW or its 2σ lower limit in units of Å. (8) Reference (O08: Ouchi et al. 2008, Hi18: Higuchi et al. 2018, J18: Jiang et al. 2018).

We adopt positions of SCUBA-2 sources detected with $>4\sigma$ total noise and then apply a simultaneous source-fitting routine available via SUSSEXtractor task in HIPE (Savage & Oliver 2007; Ott 2010). The PSF of the JCMT/SCUBA-2 image is 14″8 (Geach et al. 2017). The PSFs of the *Herschel*/SPIRE images are assumed to be Gaussian, with FWHM being 17″6, 25″1 and 35″2 at 250 μm, 350 μm, and 500 μm respectively. Total flux uncertainties are estimated by quadratically adding the instrument and confusion noise. We further fully evaluate our selection via realistic end-to-end simulation based on the galaxy model of Béthermin et al. (2017), which includes physical clustering based on abundance matching and galaxy–galaxy lensing. Using this simulation, we simulate the exact criteria we applied on our real maps. The typical flux density error is 9 mJy at 500 μm, which is in agreement with a value predicted by simulations.

Table 2
Spectroscopically Confirmed LAEs of z66OD

ID (1)	R.A. (J2000) (2)	Decl. (J2000) (3)	$z_{\rm spec}$ (4)	$\log L_{\rm Ly\alpha}$ (5)	$M_{\rm UV}$ (6)	$EW^0_{\rm Ly\alpha}$ (7)	Reference (8)
z66LAE-1	02:17:57.58	-05:08:44.64	6.595	$43.48^{+0.02}_{-0.03}$	$-21.4^{+0.6}_{-0.4}$	91^{+68}_{-29}	O10
z66LAE-2	02:18:20.69	-05:11:09.88	6.575	$42.96^{+0.07}_{-0.09}$	>-19.9	>59	O10
z66LAE-3	02:18:19.39	-05:09:00.65	6.563	$42.95^{+0.07}_{-0.09}$	$-20.8^{+0.8}_{-0.6}$	49^{+60}_{-25}	O10
z66LAE-4	02:18:43.62	-05:09:15.63	6.513	$43.04^{+0.06}_{-0.08}$	$-22.0^{+0.3}_{-0.2}$	20^{+10}_{-6}	Ha18
z66LAE-5	02:18:18.73	-05:04:12.96	6.599	$42.98^{+0.07}_{-0.08}$	$-20.9^{+0.8}_{-0.6}$	50^{+59}_{-25}	This work
z66LAE-6	02:18:27.00	-05:07:26.89	6.553	$42.99^{+0.06}_{-0.08}$	>-20.5	>66	This work
z66LAE-7	02:18:27.95	-05:06:29.89	6.597	$42.76^{+0.16}_{-0.26}$	$-21.8^{+0.6}_{-0.6}$	14^{+27}_{-8}	This work
z66LAE-8	02:17:56.99	-05:04:14.33	6.570	$42.85^{+0.09}_{-0.12}$	>-20.1	>59	This work
z66LAE-9	02:18:00.79	-05:03:30.25	6.613	$42.43^{+0.24}_{-0.57}$	>-20.2	>19	This work
z66LAE-10	02:18:00.23	-05:03:46.73	6.601	$42.60^{+0.14}_{-0.21}$	>-20.0	>42	This work
z66LAE-11	02:17:56.42	-05:16:37.96	6.559	$42.76^{+0.13}_{-0.19}$	$-21.1^{+0.8}_{-0.8}$	22^{+74}_{-13}	This work
z66LAE-12	02:17:57.30	-05:15:56.27	6.564	$42.52^{+0.20}_{-0.39}$	>-20.2	>32	This work

Note. (1) Object ID. (2) Right ascension. (3) Declination. (4) Spectroscopic redshift of the Lyα emission line. (5) Lyα luminosity in units of erg s^{-1}. (6) Absolute UV magnitude or its 2σ lower limit in units of ABmag. (7) Rest-frame Lyα EW or its 2σ lower limit in units of Å. (8) Reference (O10: Ouchi et al. 2010, Ha18: Harikane et al. 2018b).

To select red SMGs, we adopt the following criteria (Donevski et al. 2018):

$$S_{250\,\mu{\rm m}} < S_{350\,\mu{\rm m}} < S_{500\,\mu{\rm m}}, \qquad (6)$$

where $S_{250\,\mu{\rm m}}$, $S_{350\,\mu{\rm m}}$, and $S_{500\,\mu{\rm m}}$ are the *Herschel* 250 μm, 350 μm, and 500 μm fluxes, respectively. Equation (6) allows us to select $z \gtrsim 4$ SMGs whose modified blackbody emission peaks at $>500\,\mu$m (see Figure 6 in Donevski et al. 2018).[32] When using Equation (6), we adopt the following three criteria to measure the *Herschel* colors correctly. First, we use only sources whose 500 μm fluxes are measured at $>2\sigma$ levels. Second, if the sources are not detected in the 250 μm and/or 350 μm bands at the 2σ levels, we replace fluxes with 2σ flux limits. Third, we remove sources that are detected in 250 μm but not in 350 μm. After adopting these criteria and Equation (6), we reduce low-redshift interlopers using ALMA and Subaru/HSC data. We cross-match the SCUBA-2 sources with ALMA sources in archival data (see also Stach et al. 2018) within 10″, and identify ALMA counterparts of the SCUBA-2 sources if present. The ALMA data we use are taken in band 7, with typical 1σ noise levels and angular resolutions of 0.2 mJy/beam and 0″.2, respectively. We identify the ALMA counterparts of more than 70% of the SCUBA-2 sources, and most of the rest are not observed with ALMA. We then measure fluxes at the positions of the ALMA counterparts in the HSC g and r images, and exclude SCUBA-2 sources with detection at $>3\sigma$ levels in the HSC g- or r-band images (bluer than the Lyman break at $z \simeq 4$–6). Finally, we apply masks of diffraction spikes and halos from bright objects in the same fashion as for our LAEs, and obtain the final red SMG sample. We also define SMGs not selected with the above criteria as blue SMGs, which will be used for a null test. In addition, we select LAEs at $z = 5.7$ located in the sky coverage of the SCUBA-2 observation. Finally, we obtain 44 red SMGs, 673

blue SMGs, and 227 LAEs (77 spectroscopically confirmed). Note that there is no overlap between the LAEs and the ALMA sources within 2″. Because LAEs are typically dust-poor weak 850 μm and [C II]158 μm emitters (Harikane et al. 2018b), finding no overlap is reasonable. According to Geach et al. (2017), the false detection rate is $<6\%$ at the $>4\sigma$ detection. We will test whether the red SMGs are at $z = 5.7$ or not by the cross-correlation analysis later, so we do not take this false detection rate into account here.

The left panel in Figure 9 shows the locations of the red SMGs and $z = 5.7$ LAEs. We find that some of the red SMGs are clustering around z57OD (R.A. = 34.26, decl. = −5.54). We calculate the cross-correlation function (CCF) of the 227 LAEs at $z = 5.7$ and the 44 red SMGs using the estimator in Landy & Szalay (1993):

$$\omega(\theta) = \frac{D_1D_2(\theta) - D_1R_2(\theta) - R_1D_2(\theta) + R_1R_2(\theta)}{R_1R_2(\theta)}, \qquad (7)$$

where DD, DR, RD, and RR are the numbers of galaxy–galaxy, galaxy-random, random-galaxy, and random–random pairs for groups 1 and 2. We also calculate the CCF between the 77 spectroscopically confirmed LAEs and red SMGs, the CCF between the 227 LAEs and 775 blue SMGs, and angular auto-correlation functions (ACFs) of the 227 LAEs for reference. Using SCUBA-2 SMGs may have the blending bias effect on the correlation function measurements, due to confusion introduced by the coarse angular resolution (Karim et al. 2013; Stach et al. 2018). However, the effect is expected to be small, a factor of $\sim$1.2–1.3 (Cowley et al. 2017). We estimate statistical errors of the CCFs and ACF using the Jackknife estimator. We divide the samples into 47 Jackknife subsamples of about 500^2 arcsec^2, comparable to the maximum angular size of the correlation function measurements. Removing one Jackknife subsample at a time for each realization, we compute the covariance matrix as

$$C_{ij} = \frac{N-1}{N}\sum_{l=1}^{N}[\omega^l(\theta_i) - \bar{\omega}(\theta_i)][\omega^l(\theta_j) - \bar{\omega}(\theta_j)], \qquad (8)$$

---

[32] Although Donevski et al. (2018) showed that most of the galaxies lie at $z < 5$, this is because the number density of $z > 5$ SMG is low (e.g., Ivison et al. 2016).

Table 3
An Overview of High-redshift Protoclusters

Name (1)	z (2)	$N_{\rm spec}$ (3)	δ (4)	Sample (5)	Window size (6)	dz (7)	$\sigma_{\rm V}$ (8)	$M_{\rm h}$ (9)	Reference (10)
					Protocluster with $N_{\rm spec} \geqslant 10$				
z66OD	6.59	12	14.3 ± 2.1	LAE	$\pi \times 4.2^2$	0.1	670 ± 200	5.4×10^{14}	This work
HSC-z7PCC26	6.54	14	$6.8^{+6.1}_{-3.7}$	LAE	$\pi \times 4.2^2$	0.1	572	8.4×10^{14}	C17,19,Hi18
SDF	6.01	10	16 ± 7	LBG	6×6	~ 0.05	647 ± 124	$(2\text{–}4) \times 10^{14}$	To12,14
z57OD	5.69	44	11.5 ± 1.6	LAE	$\pi \times 4.2^2$	0.1	1280 ± 220	4.8×10^{14}	O05,J18,This work
SPT2349-56	4.31	14	>1000	SMG	$\pi \times 0.16^2$	0.1	408^{+82}_{-56}	1.16×10^{13}	M18
TNJ1338-1942	4.11	37	$3.7^{+1.0}_{-0.8}$	LAE/LBG	$7 \times 7 (\times 2)$	0.049	265 ± 65	$(6\text{–}9) \times 10^{14}$	V02,05,07,M04, Z05,Ov08
DRC-protocluster	4.00	10	$\sim 5.5\text{–}11.0$	SMG	0.61×0.730	$\cdots$	794	$(3.2\text{–}4.4) \times 10^{13}$	O18
PC217.96+32.3	3.79	65	14 ± 7	LAE	$\pi \times 1.2^2$	0.035	350 ± 40	$(0.6\text{–}1.3) \times 10^{15}$	Lee14,D16,S19
D4GD01	3.67	11	$\cdots$	LBG	$\pi \times 1.8^2$	~ 1	352 ± 140	$\cdots$	To16
ClJ0227-0421	3.29	19	10.5 ± 2.8	Spec	$\pi \times 6.2^2$	0.09	995 ± 343	$(1.9\text{–}3.3) \times 10^{14}$	Lem14
TNJ2009-3040	3.16	>11	$0.7^{+0.8}_{-0.6}$	LAE	7×7	0.049	515 ± 90	$\cdots$	V07
MRC0316-257	3.13	31	$2.3^{+0.5}_{-0.4}$	LAE	7×7	0.049	640 ± 195	$(3\text{–}5) \times 10^{14}$	V05,07
SSA22FLD	3.09	>15	$3.6^{+1.4}_{-1.2}$	LBG/ LAE/SMG	11.5×9	0.034	$\cdots$	$(1.0\text{–}1.4) \times 10^{15}$	S98,00,M05,Y12,U17,18
MRC0943-242	2.92	28	$2.2^{+0.9}_{-0.7}$	LAE	7×7	0.056	715 ± 105	$(4\text{–}5) \times 10^{14}$	V07
P2Q1	2.90	12	12 ± 2	Spec	7×8	0.016	270 ± 80	8.1×10^{14}	C14
MRC0052-241	2.86	37	$2.0^{+0.5}_{-0.4}$	LAE	7×7	0.054	980 ± 120	$(3\text{–}4) \times 10^{14}$	V07
HS1549	2.85	26	~ 5	LBG/SMG	$\cdots$	0.060	$\cdots$	$\cdots$	M13,Lac18
PCL1002	2.45	11	10	Spec/ LAE/SMG	$\pi \times 2.8^2$	0.016	426	$10^{14}\text{–}10^{15}$	D15,Ch15,Ca15
HS1700FLD	2.30	19	6.9 ± 2.1	BX/SMG	8×8	0.030	$\cdots$	1.4×10^{15}	S05,Lac18
PKS1138-262	2.16	15	3 ± 2	LAE/ HAE/SMG	7×7	0.053	900 ± 240	$(3\text{–}4) \times 10^{14}$	K00,04a,04b,P00,02, V07,K13,Z18
					Protocluster with $N_{\rm spec} < 10$				
A2744z8OD	8.38	1	132^{+66}_{-51}	LBG	$\pi \times 0.1^2$	~ 1	$\cdots$	9×10^{13}	I16,L17
Borg	~ 8	0	~ 4.5	LBG	2.1×2.3	~ 1	$\cdots$	$>2 \times 10^{14}$	Tr12
BDF	7.04	3	$\sim 3\text{–}4$	LBG	$\cdots$	~ 1	$\cdots$	$\cdots$	C18
HSC-z7PCC4	6.58	1	$9.0^{+6.5}_{-4.1}$	LAE	$\pi \times 4.2^2$	0.1	$\cdots$	$\cdots$	Hi18
CFHQSJ2329-0301	6.43	0	~ 6	LBG	34×27	~ 1.0	$\cdots$	$\cdots$	U10
HSC-z6PCC4	5.72	4	$9.7^{+8.5}_{-5.1}$	LAE	$\pi \times 4.2^2$	0.1	$\cdots$	$\cdots$	Hi18
HSC-z6PCC5	5.69	2	$9.7^{+8.5}_{-5.1}$	LAE	$\pi \times 4.2^2$	0.1	$\cdots$	$\cdots$	Hi18,P18
COSMOSAzTEC03	5.30	4	$\cdots$	SMG	1×1	$\cdots$	$\cdots$	$\cdots$	C11
TNJ0924-2201	5.19	6	$1.5^{+1.6}_{-1.0}$	LAE/LBG	7×7	0.073	305 ± 110	$(4\text{–}9) \times 10^{14}$	V04,07,Ov06
SDF	4.86	0	$2.0^{+1.0}_{-2.0}$	LAE	10×10	0.060	$\cdots$	$>3 \times 10^{14}$	S03
PClJ1001+0220	4.57	9	3.30 ± 0.32	Spec	11×11	0.01	1038 ± 178	2.5×10^{14}	Lem18
6C0140+326	4.41	0	8 ± 5	LAE	10×10	~ 0.04	$\cdots$	$(0.8\text{–}2.9) \times 10^{14}$	K11
D4UD01	3.24	5	$\cdots$	LBG	$\pi \times 1.6^2$	~ 1	61 ± 105	$\cdots$	To16
D1UD01	3.13	5	$\cdots$	LBG	$\pi \times 1.6^2$	~ 1	235 ± 75	$\cdots$	To16
LABd05	2.7	0	~ 2	LAE	28×11	0.165	$\cdots$	$\cdots$	P08
USS1558-003	2.53	0	$\cdots$	HAE	7×4	0.041	$\cdots$	$\cdots$	H12
4C23.56	2.48	3	$4.3^{+5.3}_{-2.6}$	HAE/SMG	7×4	0.035	$\cdots$	$\cdots$	T11,Z18
J2143-4423	2.38	0	5.8 ± 2.5	LAE	44×44	0.044	$\cdots$	$\cdots$	P04
4C10.48	2.35	0	11^{+2}_{-2}	HAE	2.5×2.5	0.046	$\cdots$	$\cdots$	H11
BoötesJ1430+3522	2.3	0	2.7 ± 1.1	LAE	$\pi \times 5^2$	0.0037	$\cdots$	1.51×10^{15}	B17

Note. (1) Object name. (2) Redshift. (3) Number of spectroscopically confirmed galaxies. (4) Galaxy overdensity. (5) Method of sample selection: (LAE) narrowband LAE, (HAE) narrowband Hα emitter, (LBG) Lyman break galaxy, (BX) "BX" galaxy of Adelberger et al. (2005), (SMG) submillimeter galaxy, (Spec) spectroscopic survey. (6) Approximate field size or the size of the structure used to calculate overdensity in units of arcmin². (7) Full width redshift uncertainty associated with the δ quoted. (8) Velocity dispersion (where available) in units of km s^{-1}. (9) Inferred total halo mass of the overdensity or expected halo mass at $z = 0$ in units of $M_\odot$. (10) Reference (B17: Bădescu et al. 2017, C11: Capak et al. 2011, C14: Cucciati et al. 2014, Ca15: Casey et al. 2015, Ch15: Chiang et al. 2015, C18: Castellano et al. 2018, C17,19: Chanchaiworawit et al. 2017, 2019, D15: Diener et al. 2015, D16: Dey et al. 2016, H11: Hatch et al. 2011, H12: Hayashi et al. 2012, Hi18: Higuchi et al. 2018, I16: Ishigaki et al. 2016, J18: Jiang et al. 2018, K00,04a,04b: Kurk et al. 2000, 2004a, 2004b, K11: Kuiper et al. 2011, K13: Koyama et al. 2013, Lee14: Lee et al. 2014, Lem14: Lemaux et al. 2014, L17: Laporte et al. 2017 Lac18: Lacaille et al. 2018, Lem18: Lemaux et al. 2018 M04: Miley et al. 2004, M05: Matsuda et al. 2005, M13: Mostardi et al. 2013, M18: Miller et al. 2018, O05: Ouchi et al. 2005, Ov06,08: Overzier et al. 2006, 2008, O18: Oteo et al. 2018, P00,02: Pentericci et al. 2000, 2002, P04: Palunas et al. 2004, P08: Prescott et al. 2008, P18: Pavesi et al. 2018, S98,00,05: Steidel et al. 1998, 2000, 2005, S03: Shimasaku et al. 2003, S19: Shi et al. 2019, T11: Tanaka et al. 2011, To12,14,16: Toshikawa et al. 2012, 2014, 2016, Tr12: Trenti et al. 2012 U10: Utsumi et al. 2010, U17,18: Umehata et al. 2017, 2018, V02,04,05,07: Venemans et al. 2002, 2004, 2005, 2007, Y12: Yamada et al. 2012, Z05: Zirm et al. 2005, Z18: Zeballos et al. 2018).
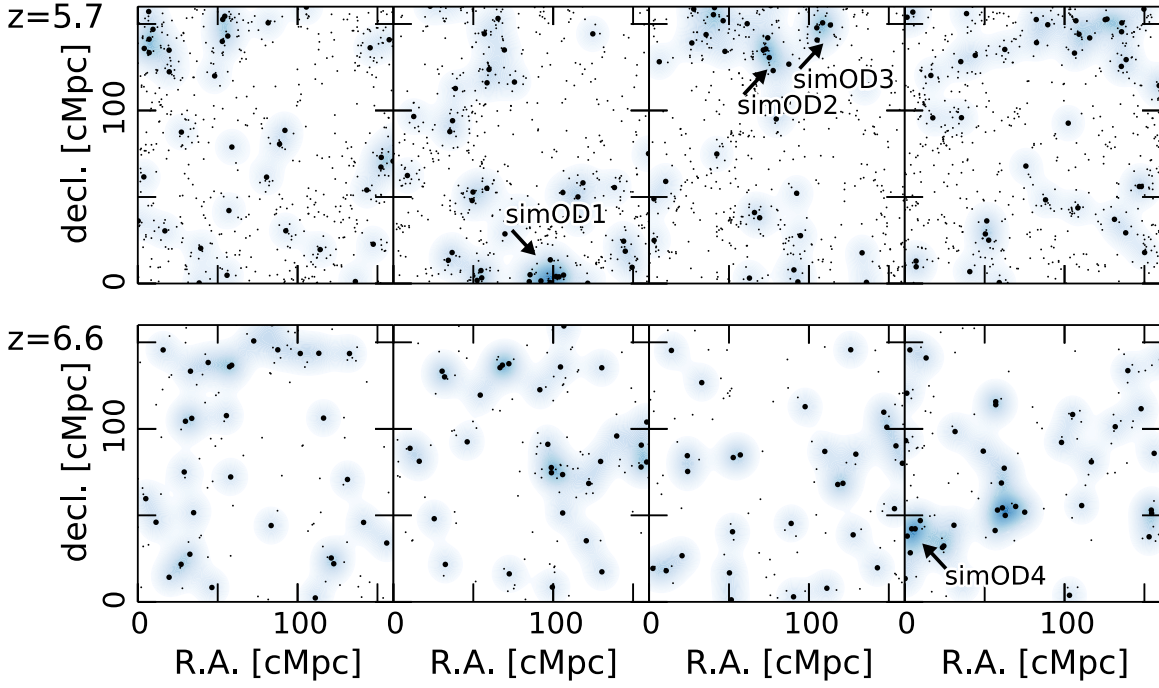
Figure 7. Upper panels: 2D map of LAEs at $z = 5.7$ for four slices in the simulation box. Each slice has the 40 cMpc depth corresponding to the narrowband width. The large black dots show the positions of the LAEs with $NB816 < 25.5$ mag. The large dots are LAEs brighter than $NB816 < 24.5$ mag. Lower panels: Same as the upper panels but at $z = 6.6$. The large dots are LAEs brighter than $NB921 = 25.0$ mag.
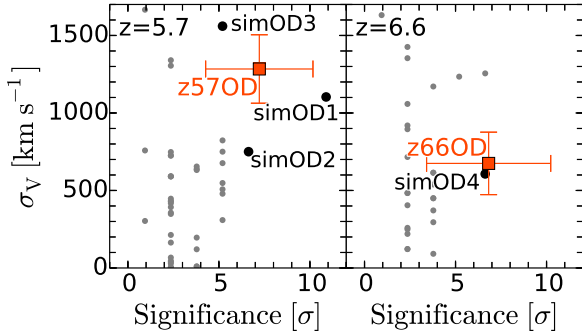

Figure 8. Velocity dispersion of LAEs of overdensities as a function of the overdensity significance for LAEs at $z = 5.7$ (left) and $z = 6.6$ (right). The red squares show z57OD (left) and z66OD (right). The black and gray circles denote the overdensities identified in the simulations. We identify three and one overdensities in simulations whose properties are similar to z57OD and z66OD, respectively.

where N is the total number of the Jackknife samples, and ω^l is the estimated CCFs or ACF from the lth realization. $\bar{\omega}$ denotes the mean CCFs and ACF. We apply a correction factor (typically ~ 1.1) given by Hartlap et al. (2007) to an inverse covariance matrix in order to compensate for the bias introduced by the statistical noise.

The calculated CCFs and ACF are presented in the right panel of Figure 9. We detect the signal of the cross-correlation between the LAEs at $z = 5.7$ and red SMGs. We evaluate the significance of the correlation by calculating the χ^2 value,

$$\chi^2 = \sum_{i,j} [\omega(\theta_i) - \omega_{\text{model}}(\theta_i)] C_{i,j}^{-1} [\omega(\theta_j) - \omega_{\text{model}}(\theta_j)], \quad (9)$$

where $\omega_{\text{model}} = 0$ for the non-detection case. We obtain $\chi^2 = 13.0$, indicating the 99.97% significance correlation. If

we use the spectroscopically confirmed LAEs, the significance level of the cross-correlation is still 96%. We do not detect the $>2\sigma$ correlation signal between the LAEs and blue SMGs, nor the LAEs and all SMGs. These significant correlations between the LAEs and red SMGs indicate that the red SMGs also trace the large-scale structure with z57OD made by the LAEs, similar to the SSA-22 protocluster at $z = 3.1$ (Tamura et al. 2009; Umehata et al. 2014). We also calculate cross-correlation functions between the LAEs at $z = 6.6$ and red SMGs, but do not detect a significant correlation signal beyond 2σ.

We evaluate the fraction of red SMGs located at $z = 5.7$. If all of the SMGs and LAEs are at $z = 5.7$, the large-scale ($\gtrsim 1$ cMpc) amplitude of the CCF between the LAEs and red SMGs is expressed as $b_{\text{LAE}} b_{\text{SMG}} \xi_{\text{DM}}$, where b_{LAE}, b_{SMG}, and ξ_{DM} are the large-scale bias of the LAE, the large-scale bias of the SMG, and the dark-matter correlation function. If some of the red SMGs are not at $z = 5.7$, the CCF amplitude will decrease by a factor of $1 - f_c$, where f_c is a fraction of the red SMGs that are not at $z = 5.7$. The large-scale amplitude of the ACF of LAEs is $b_{\text{LAE}}^2 \xi_{\text{DM}}$. Because the observed amplitudes of the CCF between the LAEs and red SMGs are comparable to that of the ACF of LAEs, we get

$$b_{\text{LAE}} b_{\text{SMG}} \xi_{\text{DM}} (1 - f_c) = b_{\text{LAE}}^2 \xi_{\text{DM}}, \quad (10)$$

and

$$(1 - f_c) = \frac{b_{\text{LAE}}}{b_{\text{SMG}}}. \quad (11)$$

The large-scale bias of LAEs at $z = 5.7$ is typically $b_{\text{LAE}} \simeq 4$ (Ouchi et al. 2018). The bias of SMGs is expected to be larger than that of LAEs ($b_{\text{SMG}} > b_{\text{LAE}}$), because SMGs are thought to be more massive than LAEs. For example, the large-scale bias of SMGs is typically ~ 3 times larger than that of LAEs
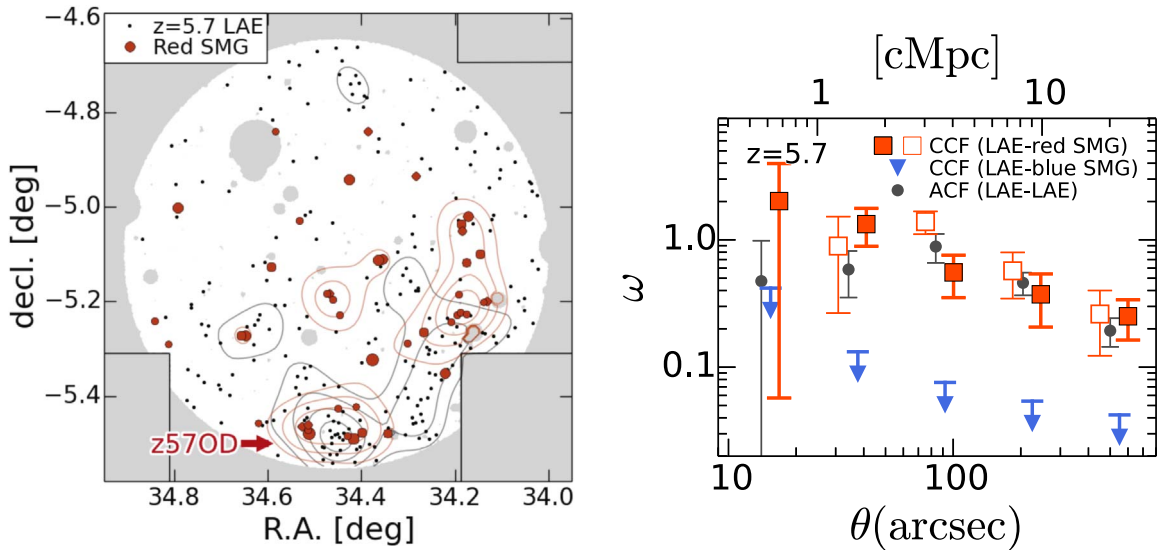
Figure 9. Left panel: locations of the red SMGs and LAEs at $z = 5.7$. The red filled circles show the red SMGs and their sizes are scaled with the 850 μm fluxes of the SMGs. The black circles are the LAEs at $z = 5.7$. The black and red contours shows the significance levels of the overdensity from 1σ to 4σ for $z = 5.7$ LAEs and red SMGs, respectively. Right panel: clustering of different populations. The red filled (open) squares show the CCFs between all the (spectroscopically confirmed) LAEs at $z = 5.7$ and red SMGs. The blue upper limits are the CCFs between the $z = 5.7$ LAEs and the blue SMGs. The black circles show the ACFs of the $z = 5.7$ LAEs for reference. We detect a significant cross-correlation signal between $z = 5.7$ LAEs and red SMGs, indicating that a large number of the red SMGs are residing at $z = 5.7$.

at $z \sim 2-3$ (e.g., Webb et al. 2003; Gawiser et al. 2007; Weiß et al. 2009; Ouchi et al. 2010). On the other hand, the effective volume of our narrowband data is $\sim 200 \times 200 \times 80$ cMpc^3. Only one halo as massive as $M_\mathrm{h} \sim 10^{13}\ M_\odot$ is expected to exist in this volume, on average (Tinker et al. 2008). Thus, we get the upper limit of the bias of the SMGs as $b_\mathrm{SMG} < b(M_\mathrm{h} = 10^{13}\ M_\odot) \simeq 14$. From the lower and upper limits obtained, $4 < b_\mathrm{SMG} < 14$, we expect that the fractions of red SMGs at $z = 5.7$ are $\sim 30\%-100\%$, suggesting that $\sim 10-40$ red SMGs are at $z = 5.7$. This is higher than the expectation from the redshift distribution in Donevski et al. (2018, their Figure 7), hinting that large numbers of red SMGs are clustering at $z = 5.7$. ALMA follow-up observations for these red SMGs are now being prepared. It is interesting that the CCF shows a strong correlation between the LAEs and the red SMGs even at the $<20''$ scale, while the ACF does not. It indicates that LAE-red SMG pairs can be more easily found in the $<20''$ scale than LAE-LAE pairs.

4.4. Star Formation Activity in z57OD and z66OD

To understand star-formation activities in z57OD and z66OD, we investigate spectral energy distributions (SEDs) of the LAEs of z57OD and z66OD. We use the images of Subaru/HSC *grizNB*816*NB*921, UKIRT/WFCAM *JHK* in the UKIDSS/UDS project (Lawrence et al. 2007), and *Spitzer*/IRAC [3.6] and [4.5] bands in the SPLASH project (P. Capak 2019, in preparation). Some LAEs are detected in the NIR images, and we can constrain SEDs of them. Regarding LAEs not detected in the NIR images, we stack images of these LAEs, and make subsamples ("non detection stack" subsamples) in z57OD and z66OD. We also stack images of all LAEs in z57OD and z66OD ("all stack" subsamples) to investigate averaged properties.

First, we run T-PHOT (Merlin et al. 2016) and generate residual IRAC images where only the LAEs under analysis are left. As high-resolution prior images in the T-PHOT run, we use HSC *grizyNB* stacked images whose PSFs are $\sim 0''.7$. Then, we visually inspect all of our LAEs and exclude sources due to the presence of bad residual features close to the targets that can possibly affect the photometry. We cut out $12'' \times 12''$ images of the LAEs in each band, and generate median-stacked images of the subsamples in each bands with IRAF task imcombine. We show the SEDs of the "all stack" subsamples at $z = 5.7$ and 6.6 in the left and center panels in Figure 10, respectively.

We generate the model SEDs at $z = 5.7$ and 6.6 using BEAGLE (Chevallard & Charlot 2016). In BEAGLE, we use the combined stellar population and photoionization models presented in Gutkin et al. (2016). Stellar emission is based on an updated version of the population synthesis code of Bruzual & Charlot (2003), while gas emission is computed with the standard photoionization code CLOUDY (Ferland et al. 2013) following the prescription of Charlot & Longhetti (2001). The IGM absorption is considered following a model of Inoue et al. (2014). In BEAGLE we vary the total mass of stars formed, ISM metallicity (Z_neb), ionization parameter (U_ion), star-formation history, stellar age, and *V*-band attenuation optical depth (τ_V), while we fix the dust-to-metal ratio (ξ_d) to 0.3 (e.g., De Vis et al. 2017), and adopt the Calzetti et al. (2000) dust extinction curve. We choose the constant star-formation history because it reproduces SEDs of high-redshift LAEs (Ono et al. 2010; Harikane et al. 2018b). The choice of the extinction law does not affect our conclusions, because our SED fittings infer dust-poor populations such as $\tau_V = 0.0-0.1$. We vary the four adjustable parameters of the model in vast ranges, $-2.0 < \log(Z_\mathrm{neb}/Z_\odot) < 0.2$ (with a step of 0.1 dex), $-3.0 < \log U_\mathrm{ion} < -1.0$ (with a step of 0.1 dex), $6.0 < \log$ (Age/yr) < 9.0 (with a step of 0.1 dex), and $\tau_V = [0, 0.05, 0.1, 0.2, 0.4, 0.8, 1.6, 2]$. We assume that the stellar metallicity
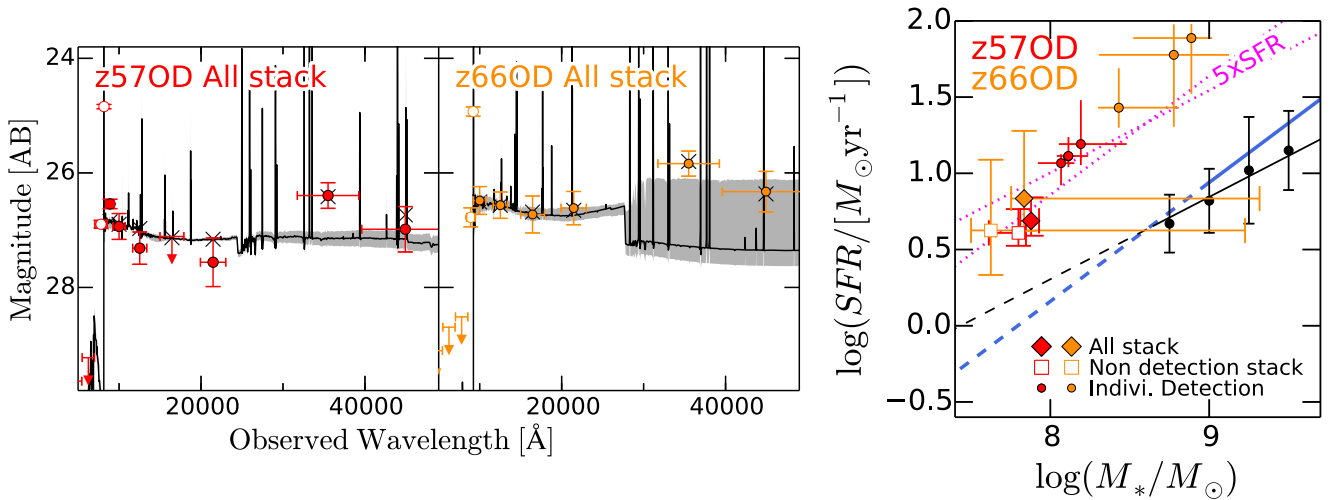
Figure 10. Left and center panels: SEDs of the "all stack" subsamples in z57OD and z66OD. The circles represent the magnitudes in the stacked images of each subsample. The filled circles are magnitudes used in the SED fittings. We do not use the magnitudes indicated with the open circles, which are affected by the IGM absorption. The dark gray lines with the gray crosses show the best-fit model SEDs, and the light gray regions show the 1σ uncertainties of the best-fit model SEDs. Right panel: SFRs of the LAEs in z57OD and z66OD as functions of the stellar mass. The red and orange diamonds (open squares) are SFRs of the all (non-detection) stack subsamples of z57OD and z66OD, respectively. SFRs of the individual LAEs detected in the NIR images are shown with the red and orange circles for z57OD and z66OD, respectively. The black line with the circles and the blue lines show results of the star-formation main sequences of Salmon et al. (2015) at $z \sim 6$ and Steinhardt et al. (2014) at $z = 4.8$–6.0, respectively. The dashed lines represent extrapolations from the ranges these studies investigate. The SFRs of the LAEs in z57OD and z66OD are ~ 5 times higher than galaxies in the main sequence.

is the same as the ISM metallicity, with interpolation of original templates. We fit our observed SEDs with these model SEDs, and derive stellar masses and SFRs of the subsamples and individuals. In the "all stack" subsample at $z = 5.7$, we can constrain the stellar mass, SFR, and metallicity. In the other subsamples, we fix the metallicity to $\log(Z/Z_\odot) = -0.6$ that is the best-fit value of the "all stack" subsample at $z = 5.7$, because we cannot constrain the metallicity due to the poor signal-to-noise ratio.

In the right panel in Figure 10, we plot the measured stellar masses and SFRs for the LAEs of z57OD and z66OD. We compare them with the star-formation main sequence that is determined with field LBGs. All the subsamples including "all stack," "non detection stack," and individual galaxies show SFRs more than ~ 5 times higher than the main-sequence galaxies in the same stellar masses, indicating that the LAEs in z57OD and z66OD are actively forming stars.

We then calculate the SFR densities of z57OD and z66OD, and compare them with the cosmic average (a.k.a. the Madau-Lilly plot). We measure the SFR densities using observed galaxies located within 1 physical Mpc (pMpc) from the centers of the overdensities, following previous studies (e.g., Clements et al. 2014; Kato et al. 2016). We find that 16 LAEs and 3 red SMGs (5 LAEs and 1 red SMG) are within the 1 pMpc-radius aperture around z57OD (z66OD). For z57OD, we measure the total SFR density of the observed LAEs and red SMGs, because the cross-correlation signal suggests that 30%–100% of the red SMGs trace the LAE large-scale structures. We assume that the average SFR of one LAE is $\sim 10 \, M_\odot \, \mathrm{yr}^{-1}$ based on the SED-fitting results. We calculate SFRs of the red SMGs from the $850 \, \mu\mathrm{m}$ fluxes assuming the redshift of $z = 5.7$, the dust temperature of $T_{\mathrm{dust}} = 40 \, \mathrm{K}$ (Rémy-Ruyer et al. 2013; Faisst et al. 2017), and the emissivity index of $\beta = 1.5$ (Chapman et al. 2005). The effect of these assumptions is not significant for our conclusions. For example, the $\Delta T_{\mathrm{dust}} = 10 \, \mathrm{K}$ or $\Delta\beta = 1.5$ difference changes the SFR
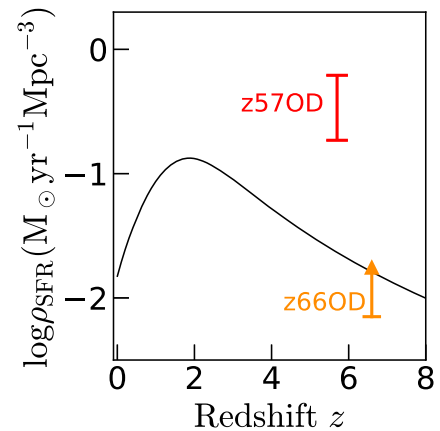

Figure 11. SFR densities. The red bar and orange lower limit are the SFR densities of z57OD and z66OD. The red bar is the summation of the observed LAEs and red SMGs with the uncertainty of the fraction of the red SMGs residing at $z = 5.7$ (30%–100%). The orange lower limit only takes into account the observed LAEs. Note that we do not include contributions from faint galaxies not detected in our data. The black curve is the cosmic average of the SFR density (Madau & Dickinson 2014). The SFR density of z57OD is more than ~ 10 times higher than the cosmic average.

density only by a factor of < 2. With this assumed temperature, the CMB effect is negligible ($<5\%$; da Cunha et al. 2013). The uncertainty of the SFR density corresponds to the uncertainty of the fraction of the red SMGs residing at $z = 5.7$ (30%–100%), because the total SFR is dominated by the SFRs of the red SMGs. For z66OD, because we do not know whether the SMGs are also at $z = 6.6$, we calculate the lower limit of the SFR density considering only the LAEs.

In Figure 11, we plot the measured SFR densities as a function of the redshift. The SFR density in z57OD is ~ 10 times higher than the cosmic average (Madau & Dickinson 2014). We do not obtain a meaningful constraint for z66OD.

These results indicate that star formation is enhanced at least in z57OD. This active star formation in the overdense region may be explained by high inflow rates in the overdense region. Recent observational studies reveal that there are tight correlations between the gas accretion rate and star-formation rate (Behroozi et al. 2018; Harikane et al. 2018a; Tacchella et al. 2018). Enhanced star formation of LAEs in the overdense region may be due to high inflow rates in overdensities whose halo is massive. Indeed, the halo masses of z57OD and z66OD are expected to be $4\text{--}10 \times 10^{11}\, M_\odot$ (see Section 4.2), larger than those of LAEs in normal fields, $1 \times 10^{11}\, M_\odot$ (Ouchi et al. 2018).

5. Summary

We have obtained 3D maps of the universe in the $\sim 200 \times 200 \times 80$ cMpc^3 volumes each at $z = 5.7$ and 6.6 based on the spectroscopic sample of 179 LAEs that accomplishes the $>80\%$ completeness down to $\log(L_{\mathrm{Ly}\alpha}/[\mathrm{erg\ s}^{-1}]) = 43.0$, based on our Keck and Gemini observations and the literature. We compare spatial distributions of our LAEs with SMGs, investigate the stellar populations, and compare our LAEs with the numerical simulations. Our major findings are summarized below.

1. The 3D maps reveal filamentary large-scale structures extending over 40 cMpc and two remarkable overdensities made of at least 44 and 12 LAEs at $z = 5.692$ (z57OD) and $z = 6.585$ (z66OD), respectively. z66OD is the most distant overdensity spectroscopically confirmed to date, with >10 spectroscopically confirmed galaxies.
2. We have identified similar overdensities to z57OD and z66OD in the simulations regarding the overdensity significance and the velocity dispersion of LAEs. The halo masses of the overdensities in simulations are $\sim(4\text{--}10) \times 10^{11}\, M_\odot$, which will grow to cluster-scale halos ($M_{\mathrm{h}} \sim 10^{14} M_\odot$) at the present day, suggesting that z57OD and z66OD are protoclusters.
3. We have selected 44 red 850 μm selected SMGs that are SMGs expected to reside at $z \simeq 4\text{--}6$ based on their red *Herschel* color, and calculated the cross-correlation functions between the LAEs and the red SMGs. We have detected 99.97% cross-correlation signal between $z = 5.7$ LAEs and the red SMGs. This significant correlation suggests that the dust-obscured SMGs are also tracing the same large-scale structures as the LAEs, which are typically dust-poor star-forming galaxies.
4. Stellar population analyses suggest that LAEs in z57OD and z66OD are actively forming stars with SFRs ~ 5 times higher than the main sequence at a fixed stellar mass. Given the significant correlation between the LAEs and the red SMGs at $z = 5.7$, the SFR density in z57OD is 10 times higher than the cosmic average (a.k.a. the Madau-Lilly plot).

ORCID iDs

Yuichi Harikane ⬤ https://orcid.org/0000-0002-6047-430X
Masami Ouchi ⬤ https://orcid.org/0000-0002-1049-6658
Seiji Fujimoto ⬤ https://orcid.org/0000-0001-7201-5066
Darko Donevski ⬤ https://orcid.org/0000-0001-5341-2162
Andreas L. Faisst ⬤ https://orcid.org/0000-0002-9382-9832
Nobunari Kashikawa ⬤ https://orcid.org/0000-0001-5493-6259
Kotaro Kohno ⬤ https://orcid.org/0000-0002-4052-2394
Akio K. Inoue ⬤ https://orcid.org/0000-0002-7779-8677
Yen-Ting Lin ⬤ https://orcid.org/0000-0001-7146-4687
Crystal L. Martin ⬤ https://orcid.org/0000-0001-9189-7818
Roderik Overzier ⬤ https://orcid.org/0000-0002-8214-7617
Ian Smail ⬤ https://orcid.org/0000-0003-3037-257X
Jun Toshikawa ⬤ https://orcid.org/0000-0001-5394-242X
Hideki Umehata ⬤ https://orcid.org/0000-0003-1937-0573
Yiping Ao ⬤ https://orcid.org/0000-0003-3139-2724
David L. Clements ⬤ https://orcid.org/0000-0002-9548-5033
Myungshin Im ⬤ https://orcid.org/0000-0002-8537-6714
Yipeng Jing ⬤ https://orcid.org/0000-0002-4534-3125
Chien-Hsiu Lee ⬤ https://orcid.org/0000-0003-1700-5740
Minju M. Lee ⬤ https://orcid.org/0000-0002-2419-3068
Lihwai Lin ⬤ https://orcid.org/0000-0001-7218-7407

14

Murilo Marinello ⓘ https://orcid.org/0000-0001-9719-4523
Tohru Nagao ⓘ https://orcid.org/0000-0002-7402-5441
Masato Onodera ⓘ https://orcid.org/0000-0003-3228-7264
Sune Toft ⓘ https://orcid.org/0000-0003-3631-7176
Wei-Hao Wang ⓘ https://orcid.org/0000-0003-2588-1265

References

Adelberger, K. L., Steidel, C. C., Pettini, M., et al. 2005, ApJ, 619, 697
Aihara, H., Arimoto, N., Armstrong, R., et al. 2018a, PASJ, 70, S4
Aihara, H., Armstrong, R., Bickerton, S., et al. 2018b, PASJ, 70, S8
Bădescu, T., Yang, Y., Bertoldi, F., et al. 2017, ApJ, 845, 172
Behroozi, P., Wechsler, R., Hearin, A., & Conroy, C. 2019, MNRAS, 488, 3143
Béthermin, M., Wu, H.-Y., Lagache, G., et al. 2017, A&A, 607, A89
Bosch, J., Armstrong, R., Bickerton, S., et al. 2017, arXiv:1705.06766
Bruzual, G., & Charlot, S. 2003, MNRAS, 344, 1000
Calzetti, D., Armus, L., Bohlin, R. C., et al. 2000, ApJ, 533, 682
Capak, P. L., Riechers, D., Scoville, N. Z., et al. 2011, Natur, 470, 233
Casey, C. M. 2016, ApJ, 824, 36
Casey, C. M., Cooray, A., Capak, P., et al. 2015, ApJL, 808, L33
Castellano, M., Pentericci, L., Vanzella, E., et al. 2018, ApJL, 863, L3
Chabrier, G. 2003, PASP, 115, 763
Chanchaiworawit, K., Guzmán, R., Rodríguez Espinosa, J. M., et al. 2017, MNRAS, 469, 2646
Chanchaiworawit, K., Guzmán, R., Salvador-Solé, E., et al. 2019, ApJ, 877, 51
Chapman, S. C., Blain, A. W., Smail, I., & Ivison, R. J. 2005, ApJ, 622, 772
Charlot, S., & Longhetti, M. 2001, MNRAS, 323, 887
Chevallard, J., & Charlot, S. 2016, MNRAS, 462, 1415
Chiang, Y.-K., Overzier, R., & Gebhardt, K. 2013, ApJ, 779, 127
Chiang, Y.-K., Overzier, R., & Gebhardt, K. 2014, ApJL, 782, L3
Chiang, Y.-K., Overzier, R. A., Gebhardt, K., et al. 2015, ApJ, 808, 37
Chiang, Y.-K., Overzier, R. A., Gebhardt, K., & Henriques, B. 2017, ApJL, 844, L23
Clements, D. L., Braglia, F. G., Hyde, A. K., et al. 2014, MNRAS, 439, 1193
Cowley, W. I., Lacey, C. G., Baugh, C. M., Cole, S., & Wilkinson, A. 2017, MNRAS, 469, 3396
Cucciati, O., Zamorani, G., Lemaux, B. C., et al. 2014, A&A, 570, A16
da Cunha, E., Groves, B., Walter, F., et al. 2013, ApJ, 766, 13
Davis, M., Faber, S. M., Newman, J., et al. 2003, Proc. SPIE, 4834, 161
De Vis, P., Gomez, H. L., Schofield, S. P., et al. 2017, MNRAS, 471, 1743
Dey, A., Lee, K.-S., Reddy, N., et al. 2016, ApJ, 823, 11
Diener, C., Lilly, S. J., Ledoux, C., et al. 2015, ApJ, 802, 31
Donevski, D., Buat, V., Boone, F., et al. 2018, A&A, 614, A33
Dressler, A. 1980, ApJ, 236, 351
Elbaz, D., Daddi, E., Le Borgne, D., et al. 2007, A&A, 468, 33
Erb, D. K., Steidel, C. C., Trainor, R. F., et al. 2014, ApJ, 795, 33
Faisst, A. L., Capak, P. L., Davidzon, I., et al. 2016, ApJ, 822, 29
Faisst, A. L., Capak, P. L., Yan, L., et al. 2017, ApJ, 847, 21
Ferland, G. J., Porter, R. L., van Hoof, P. A. M., et al. 2013, RMxAA, 49, 137
Gawiser, E., Francke, H., Lai, K., et al. 2007, ApJ, 671, 278
Geach, J. E., Dunlop, J. S., Halpern, M., et al. 2017, MNRAS, 465, 1789
Goto, T., Yamauchi, C., Fujita, Y., et al. 2003, MNRAS, 346, 601
Gott, J. R., III, Jurić, M., Schlegel, D., et al. 2005, ApJ, 624, 463
Gutkin, J., Charlot, S., & Bruzual, G. 2016, MNRAS, 462, 1757
Hamana, T., Yamada, T., Ouchi, M., Iwata, I., & Kodama, T. 2006, MNRAS, 369, 1929
Harikane, Y., Ouchi, M., Ono, Y., et al. 2018a, PASJ, 70, S11
Harikane, Y., Ouchi, M., Shibuya, T., et al. 2018b, ApJ, 859, 84
Hartlap, J., Simon, P., & Schneider, P. 2007, A&A, 464, 399
Hashimoto, T., Inoue, A. K., Mawatari, K., et al. 2019, PASJ, 71, 71
Hatch, N. A., Kurk, J. D., Pentericci, L., et al. 2011, MNRAS, 415, 2993
Hayashi, M., Kodama, T., Tadaki, K.-i., Koyama, Y., & Tanaka, I. 2012, ApJ, 757, 15
Higuchi, R., Ouchi, M., Ono, Y., et al. 2019, ApJ, 879, 28
Hu, E. M., Cowie, L. L., Capak, P., et al. 2004, AJ, 127, 563
Inoue, A. K., Hasegawa, K., Ishiyama, T., et al. 2018, PASJ, 70, 55
Inoue, A. K., Shimizu, I., Iwata, I., & Tanaka, M. 2014, MNRAS, 442, 1805
Ishigaki, M., Ouchi, M., & Harikane, Y. 2016, ApJ, 822, 5
Ivison, R. J., Lewis, A. J. R., Weiss, A., et al. 2016, ApJ, 832, 78
Jiang, L., Wu, J., Bian, F., et al. 2018, NatAs, 2, 962
Karim, A., Swinbank, A. M., Hodge, J. A., et al. 2013, MNRAS, 432, 2
Kashikawa, N., Shimasaku, K., Malkan, M. A., et al. 2006, ApJ, 648, 7

Kato, Y., Matsuda, Y., Smail, I., et al. 2016, MNRAS, 460, 3861
Kodama, T., Smail, I., Nakata, F., Okamura, S., & Bower, R. G. 2001, ApJL, 562, L9
Konno, A., Ouchi, M., Shibuya, T., et al. 2018, PASJ, 70, S16
Koyama, Y., Smail, I., Kurk, J., et al. 2013, MNRAS, 434, 423
Kuiper, E., Hatch, N. A., Venemans, B. P., et al. 2011, MNRAS, 417, 1088
Kurk, J. D., Pentericci, L., Overzier, R. A., Röttgering, H. J. A., & Miley, G. K. 2004a, A&A, 428, 817
Kurk, J. D., Pentericci, L., Röttgering, H. J. A., & Miley, G. K. 2004b, A&A, 428, 793
Kurk, J. D., Röttgering, H. J. A., Pentericci, L., et al. 2000, A&A, 358, L1
Lacaille, K., Chapman, S., Smail, I., et al. 2019, MNRAS, 488, 1790
Lahav, O., Lilje, P. B., Primack, J. R., & Rees, M. J. 1991, MNRAS, 251, 128
Landy, S. D., & Szalay, A. S. 1993, ApJ, 412, 64
Laporte, N., Ellis, R. S., Boone, F., et al. 2017, ApJL, 837, L21
Lawrence, A., Warren, S. J., Almaini, O., et al. 2007, MNRAS, 379, 1599
Lee, K.-S., Dey, A., Hong, S., et al. 2014, ApJ, 796, 126
Lemaux, B. C., Cucciati, O., Tasca, L. A. M., et al. 2014, A&A, 572, A41
Lemaux, B. C., Le Fèvre, O., Cucciati, O., et al. 2018, A&A, 615, A77
Lewis, I., Balogh, M., De Propris, R., et al. 2002, MNRAS, 334, 673
Madau, P., & Dickinson, M. 2014, ARA&A, 52, 415
Matsuda, Y., Yamada, T., Hayashino, T., et al. 2005, ApJL, 634, L125
Merlin, E., Bourne, N., Castellano, M., et al. 2016, A&A, 595, A97
Miley, G. K., Overzier, R. A., Tsvetanov, Z. I., et al. 2004, Natur, 427, 47
Miller, T. B., Chapman, S. C., Aravena, M., et al. 2018, Natur, 556, 469
Mostardi, R. E., Shapley, A. E., Nestor, D. B., et al. 2013, ApJ, 779, 65
Oke, J. B., & Gunn, J. E. 1983, ApJ, 266, 713
Ono, Y., Ouchi, M., Shimasaku, K., et al. 2010, ApJ, 724, 1524
Oteo, I., Ivison, R. J., Dunne, L., et al. 2018, ApJ, 856, 72
Ott, S. 2010, in ASP Conf. Ser. 434, Astronomical Data Analysis Software and Systems XIX, ed. Y. Mizumoto, K.-I. Morita, & M. Ohishi (San Francisco, CA: ASP), 139
Ouchi, M., Harikane, Y., Shibuya, T., et al. 2018, PASJ, 70, S13
Ouchi, M., Shimasaku, K., Akiyama, M., et al. 2005, ApJL, 620, L1
Ouchi, M., Shimasaku, K., Akiyama, M., et al. 2008, ApJS, 176, 301
Ouchi, M., Shimasaku, K., Furusawa, H., et al. 2010, ApJ, 723, 869
Overzier, R. A. 2016, A&ARv, 24, 14
Overzier, R. A., Bouwens, R. J., Cross, N. J. G., et al. 2008, ApJ, 673, 143
Overzier, R. A., Guo, Q., Kauffmann, G., et al. 2009, MNRAS, 394, 577
Overzier, R. A., Miley, G. K., Bouwens, R. J., et al. 2006, ApJ, 637, 58
Palunas, P., Teplitz, H. I., Francis, P. J., Williger, G. M., & Woodgate, B. E. 2004, ApJ, 602, 545
Pavesi, R., Riechers, D. A., Sharon, C. E., et al. 2018, ApJ, 861, 43
Pentericci, L., Kurk, J. D., Carilli, C. L., et al. 2002, A&A, 396, 109
Pentericci, L., Kurk, J. D., Röttgering, H. J. A., et al. 2000, A&A, 361, L25
Planck Collaboration, Ade, P. A. R., Aghanim, N., et al. 2016, A&A, 594, A13
Prescott, M. K. M., Kashikawa, N., Dey, A., & Matsuda, Y. 2008, ApJL, 678, L77
Rémy-Ruyer, A., Madden, S. C., Galliano, F., et al. 2013, A&A, 557, A95
Salmon, B., Papovich, C., Finkelstein, S. L., et al. 2015, ApJ, 799, 183
Savage, R. S., & Oliver, S. 2007, ApJ, 661, 1339
Shi, K., Huang, Y., Lee, K.-S., et al. 2019, ApJ, 879, 9
Shibuya, T., Ouchi, M., Harikane, Y., et al. 2018a, PASJ, 70, S15
Shibuya, T., Ouchi, M., Konno, A., et al. 2018b, PASJ, 70, S14
Shimasaku, K., Hayashino, T., Matsuda, Y., et al. 2004, ApJL, 605, L93
Shimasaku, K., Ouchi, M., Okamura, S., et al. 2003, ApJL, 586, L111
Stach, S. M., Smail, I., Swinbank, A. M., et al. 2018, ApJ, 860, 161
Steidel, C. C., Adelberger, K. L., Dickinson, M., et al. 1998, ApJ, 492, 428
Steidel, C. C., Adelberger, K. L., Shapley, A. E., et al. 2000, ApJ, 532, 170
Steidel, C. C., Adelberger, K. L., Shapley, A. E., et al. 2005, ApJ, 626, 44
Steinhardt, C. L., Speagle, J. S., Capak, P., et al. 2014, ApJL, 791, L25
Tacchella, S., Bose, S., Conroy, C., Eisenstein, D. J., & Johnson, B. D. 2018, ApJ, 868, 92
Tamura, Y., Kohno, K., Nakanishi, K., et al. 2009, Natur, 459, 61
Tanaka, I., De Breuck, C., Kurk, J. D., et al. 2011, PASJ, 63, 415
Tanaka, M., Goto, T., Okamura, S., Shimasaku, K., & Brinkmann, J. 2004, AJ, 128, 2677
Tinker, J., Kravtsov, A. V., Klypin, A., et al. 2008, ApJ, 688, 709
Toshikawa, J., Kashikawa, N., Ota, K., et al. 2012, ApJ, 750, 137
Toshikawa, J., Kashikawa, N., Overzier, R., et al. 2014, ApJ, 792, 15
Toshikawa, J., Kashikawa, N., Overzier, R., et al. 2016, ApJ, 826, 114
Tran, K.-V. H., Papovich, C., Saintonge, A., et al. 2010, ApJL, 719, L126
Trenti, M., Bradley, L. D., Stiavelli, M., et al. 2012, ApJ, 746, 55
Umehata, H., Hatsukade, B., Smail, I., et al. 2018, PASJ, 70, 65
Umehata, H., Matsuda, Y., Tamura, Y., et al. 2017, ApJL, 834, L16

Umehata, H., Tamura, Y., Kohno, K., et al. 2014, MNRAS, 440, 3462
Umehata, H., Tamura, Y., Kohno, K., et al. 2015, ApJL, 815, L8
Utsumi, Y., Goto, T., Kashikawa, N., et al. 2010, ApJ, 721, 1680
Venemans, B. P., Kurk, J. D., Miley, G. K., et al. 2002, ApJL, 569, L11
Venemans, B. P., Röttgering, H. J. A., Miley, G. K., et al. 2005, A&A, 431, 793
Venemans, B. P., Röttgering, H. J. A., Miley, G. K., et al. 2007, A&A, 461, 823

Venemans, B. P., Röttgering, H. J. A., Overzier, R. A., et al. 2004, A&A, 424, L17
Webb, T. M., Eales, S., Foucaud, S., et al. 2003, ApJ, 582, 6
Weiß, A., Kovács, A., Coppin, K., et al. 2009, ApJ, 707, 1201
Yamada, T., Matsuda, Y., Kousai, K., et al. 2012, ApJ, 751, 29
Zeballos, M., Aretxaga, I., Hughes, D. H., et al. 2018, MNRAS, 479, 4577
Zirm, A. W., Overzier, R. A., Miley, G. K., et al. 2005, ApJ, 630, 68